Determination of the Domain Structure of FePd Thin Films and Its Relation to the Magneto-Resistance Effects

Master thesis of

Jianwei Ye

at the Jülich Centre for Neutron Science, Institut of Quantum Materials and Collective Phenomena
in Forschungszentrum Jülich

Supervisor:	Prof. Dr. Thomas Brückel
Second supervisor:	Prof. Dr. Regina Dittmann
Advisor:	Dr. Emmanuel Kentzinger

01. July 2020 – 31. December 2020

Contents

1 Introduction

1.1 Motivation

The cubic crystal symmetry of the FePd thin film transforms into a tetragonal crystal symmetry in the $L1_0$-ordered phase. The $L1_0$-ordered phase leads to a magnetic easy axis along c-direction and out-of-plane magnetization, because $L1_0$-ordered ferromagnetic phases have their easy axis along the high symmetry axis of the structure [1].
Due to strong perpendicular magnetic anisotropy(PMA), magnetic domains of the $L1_0$-ordered FePd thin film exhibit a periodical arrangement with alternative up and down magnetization that is perpendicular to the thin film surface [2]. Therefore, FePd thin film with $L10$ phase is a competitive candidate for high density recording media and ferromagnetic dielectric medium for ferromagnetic random access memory(FeRAM) [3]. Besides, FePd thin film is also a suitable system for the investigation of the domain wall resistance, because the strong perpendicular magnetic anisotropy reduces the anisotropic magnetoresistance during the transport measurements [4].
The magnetic domain structure of FePd thin films and its switching process play a very important role in both high density recording and FeRAM, since the directions of the magnetization represent "0" or "1" respectively and the writing as well as the erasing are dependent on the domain switching process. Therefore, investigating the domain structure and its switching mechanism is very important for industrial applications and related academic researches.

1.2 Goal

In order to investigate the domain structure and its switching mechanism, the material system for corresponding characterizations need to be prepared first. Among several common thin film growth methods, the oxide molecular beam epitaxy(OMBE) is particularly suitable for preparing FePd thin films required for the investigation, since the alternative Fe and Pd atom planes is the prerequisite for the formation of $L1_0$-order.
In this project, two FePd thin film samples were grown by the OMBE system with two different growth modes. The crystalline structure of those samples were characterized using x-ray diffraction(XRD) and wide-angle x-ray scattering(WAXS). Surface roughness and in-plane domain patterns are measured by atomic force microscopy(AFM) and magnetic force microscopy(MFM). Combining with domain patterns and magnetization measurements performed both in-plane and out-of-plane, a basic model of the lateral domain structure can be built. Since the magnetic domain wall structure is related to many physical properties such as the resistivity of thin films, the switching process of

magnetic domains can be analyzed indirectly by measuring the magnetoresistance in an applied oscillating magnetic field.

2 Theory

The FePd system exhibits a phase transition at around 920 K between a disordered face-center-cubic phase and an $L1_0$ ordered tetragonal structure [5]. This ordered structure is characterized by alternating Fe and Pd atomic plane along (001) direction and shows interesting properties such as high perpendicular magnetic anisotropy [6]. In order to investigate the magnetic domain structure of the FePd layer, the theory of ferromagnetism should be introduced first.

2.1 Ferromagnetism

A ferromagnet has a spontaneous magnetization even in the absence of an applied field. For an isotropic without strong easy-axis anisotropy, the appropriate Hamiltonian for a ferromagnet in an applied field **B** is

$$\hat{\mathcal{H}} = -\sum_{ij} J_{ij}\mathbf{S}_i \cdot \mathbf{S}_j + g\mu_B \sum_j \mathbf{S}_j \cdot \mathbf{B} \tag{2.1}$$

where J_{ij} is the exchange constant for nearest neighbours and it is always positive for ferromagnetic system, g is the dimensionless magnetic moment characterizing the magnetic moment and angular moment of an electron, μ_b is the Bohr magneton and B is the applied field. A Weiss molecular field model is introduced to rewrite equation 2.1

$$\mathbf{B}_{mf} = -\frac{2}{g\mu_{\mathbf{B}}} \sum_j J_{ij}\mathbf{S}_j \tag{2.2}$$

so that the effective Hamiltonian can be written as

$$\hat{\mathcal{H}} = g\mu_B \sum_i \mathbf{S}_i \cdot (\mathbf{B} + \mathbf{B}_{mf}) \tag{2.3}$$

The ferromagnetic system can be treated as a simple paramagnet but with a magnetic field $\mathbf{B} + \mathbf{B}_{mf}$. The moments can be aligned by the internal molecular field at low temperature. As the temperature increases, thermal fluctuations begin to destroy the magnetization that is generated because of the internal molecular field, so that the ferromagnet exhibits a phase transition at the Curie temperature T_C.
For materials with large T_C such as Fe, the internal molecular field needs to be about 10^3 T, which is impossible if one only considers dipole fields. A theory of exchange interaction was proposed by Heisenberg. It shows that it was the exchange interaction, which is responsible for the large internal molecular field [7].

2.1.1 Magnetic Domains

In 1907, Weiss proposed domain theory to explain ferromagnetism [8]. According to this theory, a single crystal of ferromagnet contains a number of small regions called domains, and each of them is magnetized to saturation value. The moments in one domain are oriented in a particular direction but the directions of the magnetization of different domains vary from domain to domain, so that the magnetization of the whole material is zero in the absence of an external magnetic field.
Different domains are separated by domain walls, which can be classified according to the angle between the magnetization in two domains as shown in figure 2.1.

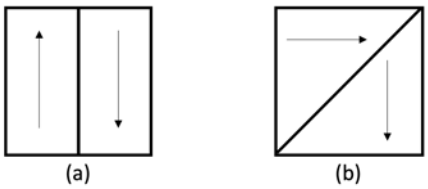

Figure 2.1: (a) 180° domain wall and (b) 90° domain wall.

Most of 180° domain walls are Bloch walls. in which the magnetization rotates 180° in a plane parallel to the plane of the wall as shown in figure 2.5(a). The Néel wall is another possible configuration and in this configuration the magnetization rotates 180° or 90° in a plane that is perpendicular to the plane of the wall as shown in figure 2.5(b).

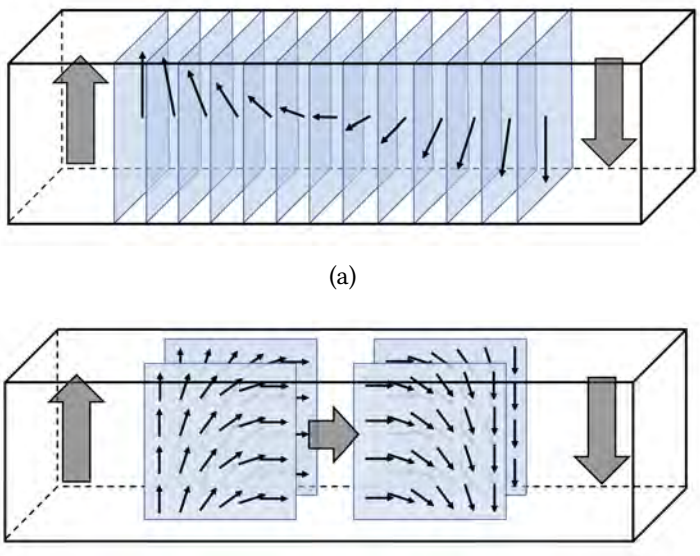

Figure 2.2: Magnetizations in (a) Bloch wall rotate in planes that are parallel to the plane of the wall. Magnetizations in (b) Néel Wall rotate in planes that are perpendicular to the plane of the wall.

In a ferromagnet it costs energy to rotate the neighbouring spins and the formation of a

domain wall also costs energy. Domains still form, because they minimize the energy of the dipolar stray fields. The dipolar energy is minimized by breaking the material into several domains as shown in figure 2.3(a) and figure 2.3(b), however, the formation of a domain wall costs additional energy. Therefore, the domain formation is a balance between the dipolar energy and the energy cost of magnetization rotation. Figure 2.3 shows three different domain structures.
The first one in figure 2.3(a) is a ferromagnet with a single domain. It has no domain wall but the system has a large dipolar energy. The dipolar energy can be reduced by forming two domains with head-to-tail magnetization as shown in figure 2.3(b). In order to save the dipolar energy further, the so-called closure domain structure can be formed as shown in figure 2.3(c).

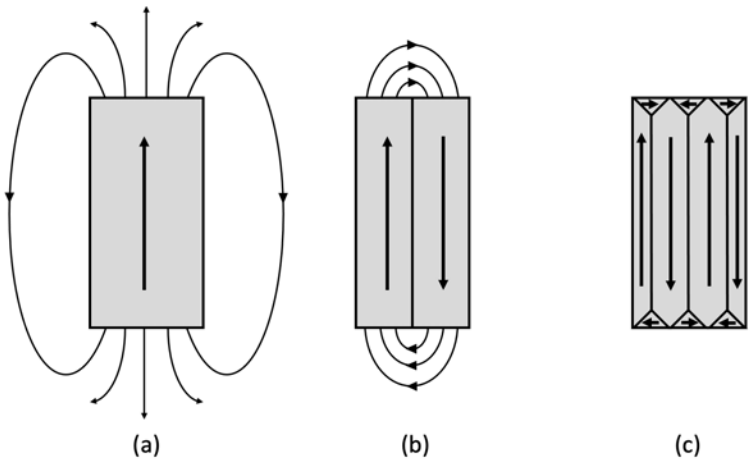

Figure 2.3: The dipolar field of a sample which is uniformly magnetized (a), divided into two 180° domains (b), with a simple closure domain structure (c). The sketch is inspired from [7].

2.1.2 Magnetic Anisotropy

Magnetic anisotropy means that there is a nonuniform coercivity in different directions for a magnetic material. The tendency for magnetization to lie along an easy axis is represented by the energy density term

$$E_a = K_1 \sin^2 \theta \tag{2.4}$$

with the angle between the magnetization and the anisotropy axis θ and the constant K_1. There are three main sources of the anisotropy: shape anisotropy, magnetocrystalline anisotropy and induced anisotropy.
The shape anisotropy originates from the long-range dipolar interaction, so that the shape anisotropy is dependent on the shape of the sample. In a thin film system, the dipolar energy density is given by

$$E_{sh} = \frac{1}{2}\mu_0 M_s^2 \cos^2 \theta \tag{2.5}$$

where M_s is the saturation magnetization and θ is the angle between the magnetization and the plane normal [9]. Hence, the magnetization of a thin film sample is often in-plane.
The magnetocrystalline anisotropy is an intrinsic property because it is dependent on the crystalline symmetry. Its origin is in the crystal-field interaction and spin-orbit coupling, or else the interatomic dipole-dipole interaction [10].
The induced anisotropy contains the anisotropy induced by applied stress or some special atomic texture.

2.2 FePd Thin Film

Epitaxial FePd thin films with $L1_0$-ordered structure have drawn a lot of attention for high density memory media because of their high perpendicular magnetic anisotropy (PMA) [**2012a**]. In $L1_0$-ordered FePd thin film sample, the Fe and Pd atom plane stack alternatively along the c-axis of its fcc crystalline structure as shown in figure 2.4.

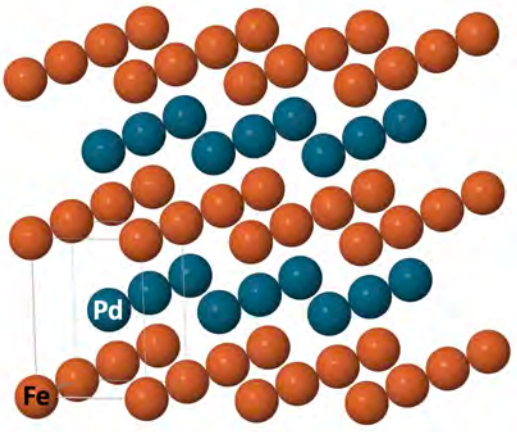

Figure 2.4: Alternative atomic stack of FePd with $L1_0$-ordered structure [11]. The 3D-model of the lattice structure is exported from [12].

Growth temperature that is higher than 500 $^\circ C$ is typically required for $L1_0$ ordering, while the crystalline structure is disordered fcc when the deposition temperature is lower [13], so that the magnetic easy axis lies in the plane of the thin film sample. The difference in the magnetic anisotropy leads to different domain structures for $L1_0$-ordered and disordered fcc FePd thin films.
The formation of magnetic domains is strongly dependent on the strength of the magnetic anisotropy. The sample with high perpendicular magnetic anisotropy (PMA) usually exhibits a maze-like magnetic domain pattern, while low PMA leads to a parallel striped domain pattern as shown in figure 2.5.

For the sample with low PMA, the in-plane component of magnetization is very strong in the demagnetized state, which leads to closure domains as explained in figure 2.3 to reduce the dipolar energy [15]. Since magnetic moments tend to be parallel to each

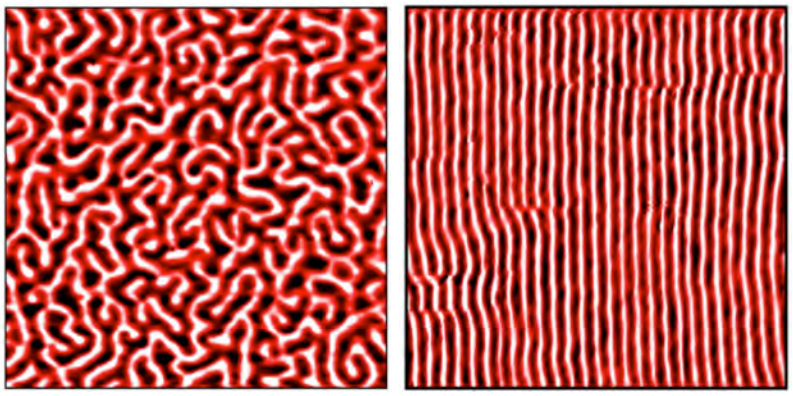

(a) (b)

Figure 2.5: (a) Maze magnetic domain pattern of the sample with high PMA and (b) parallel striped domain pattern of the sample with low PMA. Figures are taken from [14].

other, the magnetic domains of the sample with low PMA are spontaneously aligned and show a parallel striped domain pattern [16].

3 Experimental Methods

In this chapter some experimental instruments and their basic operations will be briefly discussed. The films were grown by oxide molecular beam epitaxy (OMBE) equipped with a low-energy electron diffraction (LEED), a reflection high-energy electron diffraction (RHEED), which is a typical tool for in-situ characterization. Structural properties were determined by X-ray diffractometer. Magnetization and resistivity were measured using a magnetic property measurement system (MPMS) and a physical property measurement system (PPMS), respectively.

3.1 Sample Growth

3.1.1 Oxide Molecular Beam Epitaxy (OMBE)

The system used to grow FePd thin film is a M600 oxide molecular beam epitaxy (OMBE) system from DCA instruments. Figure 3.1 shows the basic components of the OMBE system, which includes a load lock, a buffer line and a main chamber.

The samples can be loaded to the trolley in the load lock by opening the quick access door after venting the load lock. The gate valve between the load lock and the buffer line can be opened after the load lock is pumped down so that the loaded trolley can be transferred into the buffer line. Here the sample holder can be either transferred further into the main chamber through the transfer arm or moved to the LEED station and a LEED characterization performed.

A simplified structure of the OMBE main chamber is shown in figure 3.2. Samples are first loaded from the transfer arm onto the manipulator, where the heater element is located. There are six effusion cells and two electron guns (e-gun) available in the main chamber. Each evaporator unit has its own shutter, which can be controlled individually to realize different growth modes. The growth rate is monitored and adjusted with the aid of a quartz crystal microbalance (QCB) before starting the growth process. An increase in mass load on the quartz surface results in a decrease of resonant frequency [18], which is know as Sauerbrey effect, the growth rate therefore can be monitored quantitatively by tracking the decrease of resonant frequency and adjusted by changing the effusion cell temperature. A cryo-shield is installed on the top of the main chamber. The liquid nitrogen flow should be started if any component of the main chamber is heated higher than 600 °C. The cryo-shield with liquid nitrogen can also capture atoms and decrease the pressure inside the chamber down to 10^{-11} torr.

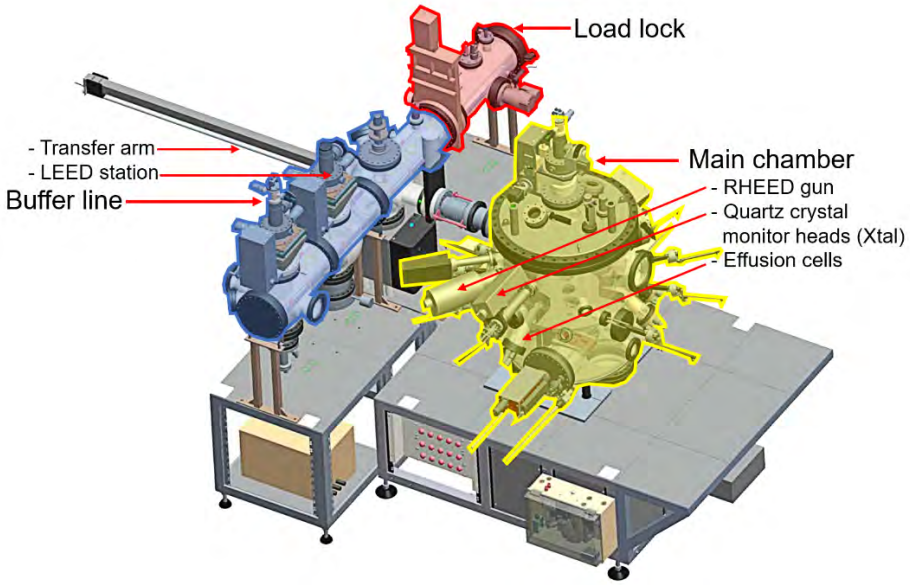

Figure 3.1: Schematic setup of the OMBE system, the 3D-figure is taken from [17]. Two valves separate the system into three chambers, the load lock for loading and removing samples, the buffer line for sample transfer and LEED characterization, and the main chamber for thin film growth and in-situ RHEED characterization.

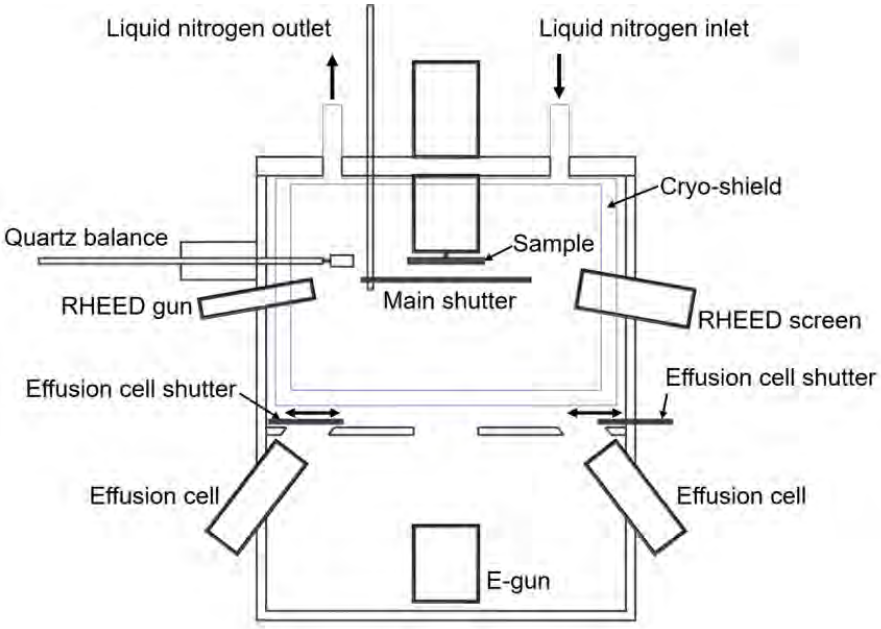

Figure 3.2: Schematic cross section of the OMBE main chamber. The sample is mounted upside-down on a manipulator with heater. Effusion cells and E-guns can be closed with their shutters and a main shutter is installed below the sample that can be closed while adjusting the growth rates.

3.1.2 Reflection High Energy Electron Diffraction RHEED

Reflection High Energy Electron Diffraction (RHEED) with the electron beam energy of 10-100 keV is a surface sensitive technique. RHEED is used to analyze structures of crystal surfaces at atomic levels and also to in-situ monitor growth processes of thin films [19].

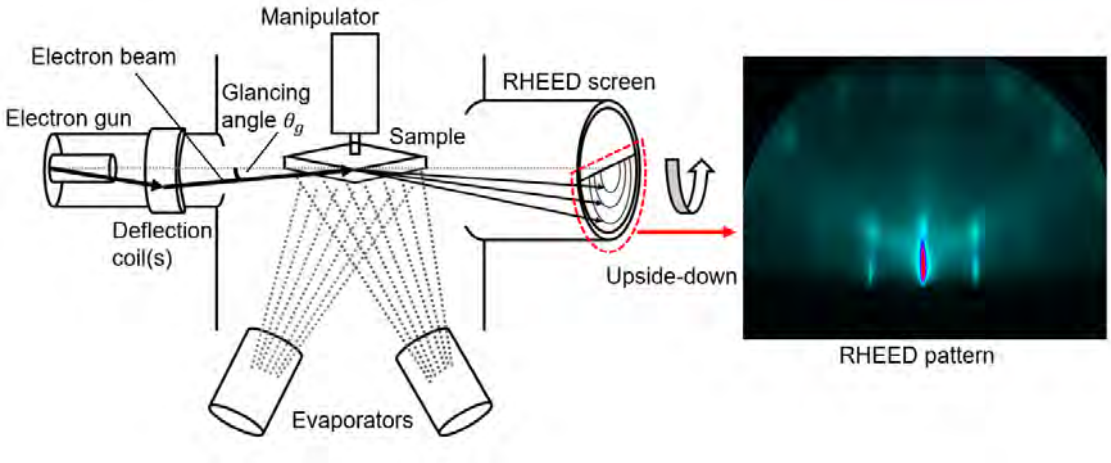

Figure 3.3: Schematic setup of a RHEED. A high energy electron beam hits the sample with a small glancing angle θ_g. Electrons can interfere constructively to form a diffraction pattern on the RHEED screen to enable the in-situ characterization during the sample growth.

As shown in figure 3.3, a high energy electron beam was focused on the sample surface with a glancing angle θ_g, which should be between 0.5-6 °. Because of the small glancing angle the electron beam interacts with a 1-3 mm area along the beam on the sample surface. RHEED patterns, therefore, show the averaged information in such an area. The RHEED pattern was observed on the fluorescence screen and it can be recorded through a CCD camera for later analyzing and in-situ monitoring. RHEED patterns are usually used for having a rough estimation of the surface state, which is always not ideal. The surfaces with domains, polycrystalline, 3D islands or terraces structures could result in different RHEED patterns.
Depending on the growth conditions there are several different growth modes. If the film grows layer by layer, the surface state switches between flat surface and terraces structure, which results in the oscillation of intensities during the growth. For island growth the electron beam is not only reflected from surface, but also diffracted through the 3D island, which leads to a bulk-like diffraction pattern. Therefore, RHEED is a powerful in-situ characterization method.

3.1.3 Low Energy Electron Diffraction LEED

Low energy electron diffraction (LEED) is another technique to analyze the crystal structure of the sample surface. LEED is surface sensitive because electrons that are used as probes have low energies between 50 eV and 300 eV, so that they can only penetrate

a few atomic layers into the sample surface. Figure 3.4 shows the basic structure of a LEED instrument. Electrons are accelerated and focused onto the sample, which is mounted upside-down above the fluorescent screen. The electrons are backscattered by the sample and a diffraction pattern is formed. A retarding grid that acts as an energy filter was installed in front of the screen to block inelastic scattered electrons that have low energy. Finally, electrons are accelerated up to 6 keV to excite the fluorescent screen [20].

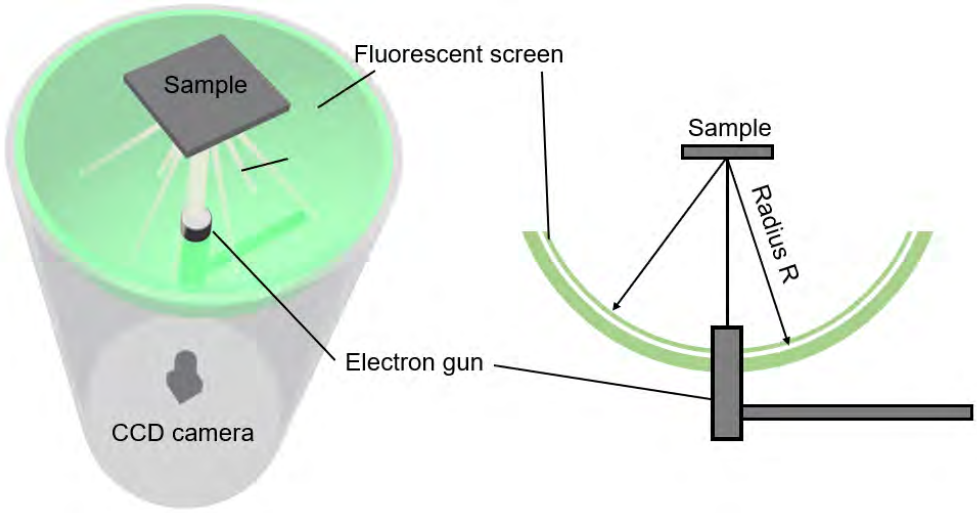

Figure 3.4: Schematic geometry of a LEED instrument. A low energy electron beam was generated and accelerated by the electron gun installed underneath the LEED screen. The electron beam hits the sample and the backscattered electrons form the diffraction pattern on the fluorescent screen.

3.2 In-house Characterization Methods

3.2.1 X-ray Refractometer

Both x-ray refractomety (XRR) and x-ray diffractometry (XRD) were performed using a Bruker D8 refractometer. A simplified setup of the instrument is shown in figure 3.5. The system uses a copper tube as x-ray source, which has a wavelength of 1.54055Å. The radiation beam is collimated and selected by a Göbel mirror with a following slit system S1 and S2 as well as a channel cut monochromator. There is another Göbel mirror in the detector arm to focus the scattered beam on the resolution slit S4.

The layer thickness and roughness were investigated in the reflectometry mode by fitting the data using the GenX program [22]. The out-of-plane crystalline structure of the prepared thin film was characterized in the diffraction mode.

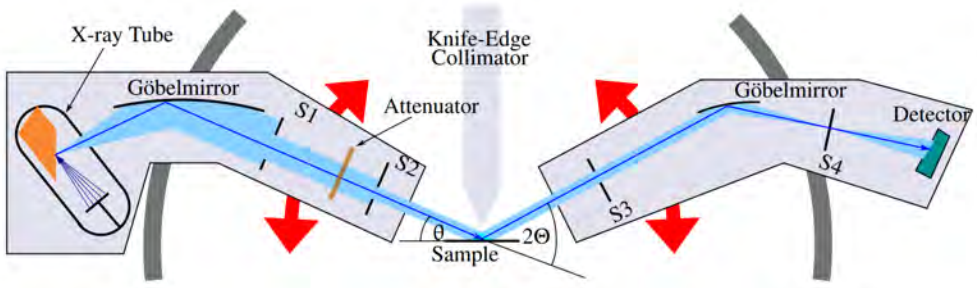

Figure 3.5: Schematic geometry of the x-ray refractometer. The sketch is taken from [21]

3.2.2 Wide-Angle X-ray Scattering

The wide-angle x-ray scattering (WAXS) is an x-ray scattering characterization method installed on the GALAXI platform. A schematic geometry of the GALAXI platform is shown in figure 3.6. The x-ray source of the GALAXI is the METALJET source built by Bruker AXS and it has a wavelength of 1.34 Å.

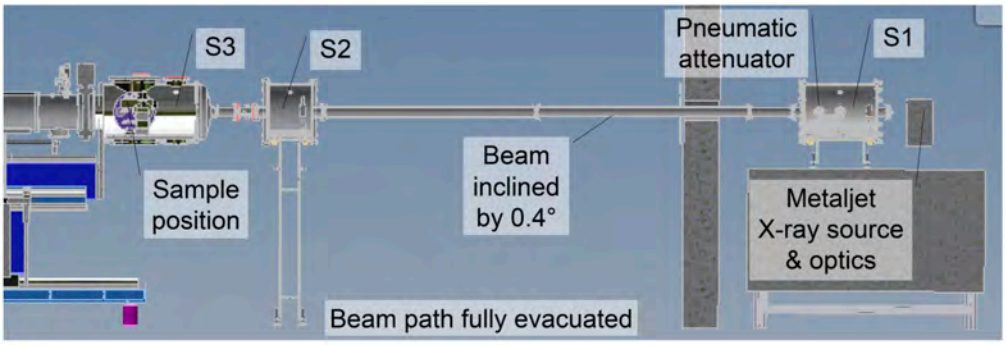

Figure 3.6: Schematic geometry of the GALAXI platform. The sketch is taken from [23]

The sample is mounted on a horizontal rotator in the chamber S3 as shown in figure 3.7(a). A Mythen wide-angle detector is installed in S3 chamber with a specific orientation, so that the value of 2θ of those lattice parameters needed to be investigated are in the range between the minimum $2\theta_1$ and maximum $2\theta_2$ of the detector as can be seen in figure 3.7(a)

The sample can be rotated by the horizontal rotator, so that the data of x-ray scattering with a 2θ range between $2\theta_1$ and $2\theta_2$ can be recorded at various ω values between 0 ° and 360 °. At every single angle of ω, the Mythen wide-angle detector records the intensities of x-ray diffraction from $2\theta_1$ to $2\theta_2$. These intensities correspond to different scattering vector Q in the reciprocal space as shown in figure 3.7(b). Therefore, a large range of the reciprocal space of the sample can be plotted from a large data set obtained at different ω.

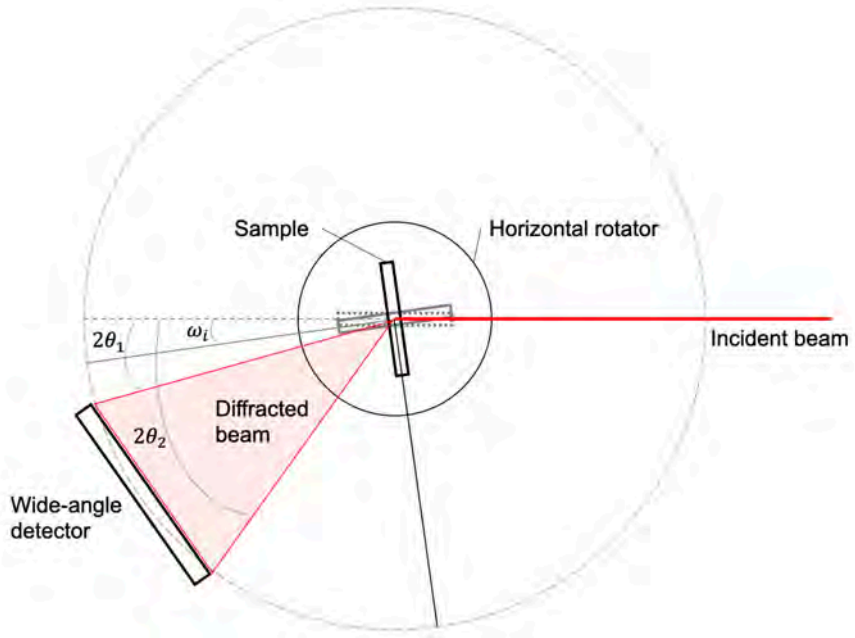

(a) Schematic geometry of the WAXS.

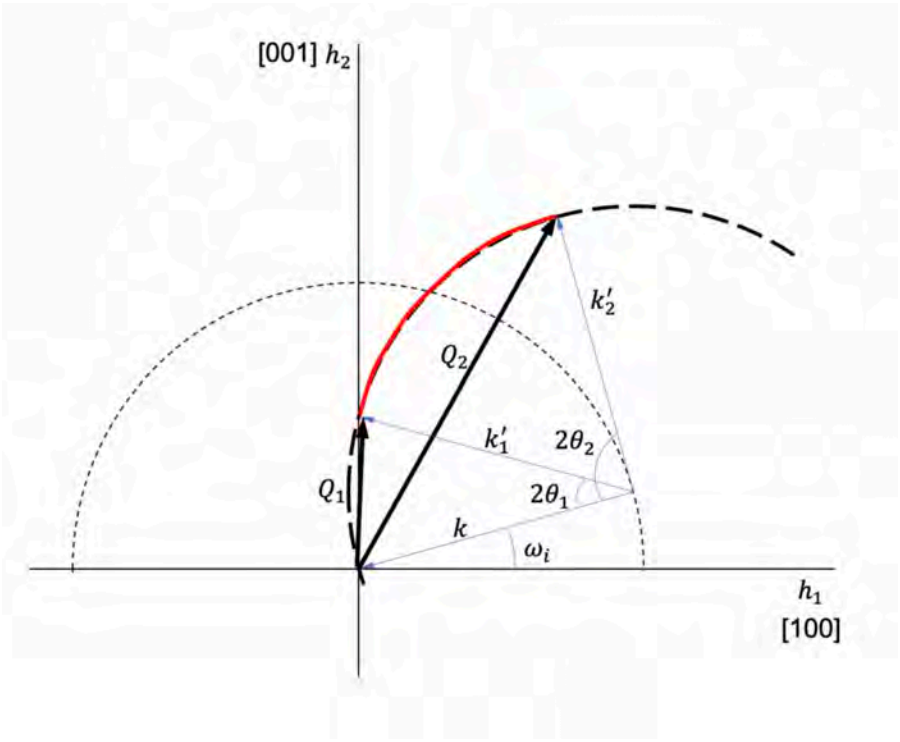

(b) The calculation of the reciprocal data form the WAXS data. ω_i is the rotation angle of the sample, $\mathbf{k}$ is the incident wave vector, $\mathbf{k}_1'$ and $\mathbf{k}_2'$ are diffracted wave vectors at $2\theta_1$ and $2\theta_2$, $\mathbf{Q}_1$ and $\mathbf{Q}_2$ are the scattering vectors at $2\theta_1$ and $2\theta_2$.

Figure 3.7: A simplified principle of the WAXS.

3.2.3 Atomic Force Microscope and Magnetic Force Microscopy

An Agilent Technologies 5400 Atomic Force Microscope (AFM) with a magnetic tip has been used for both surface AFM analyzing and magnetic domain characterization simultaneously.

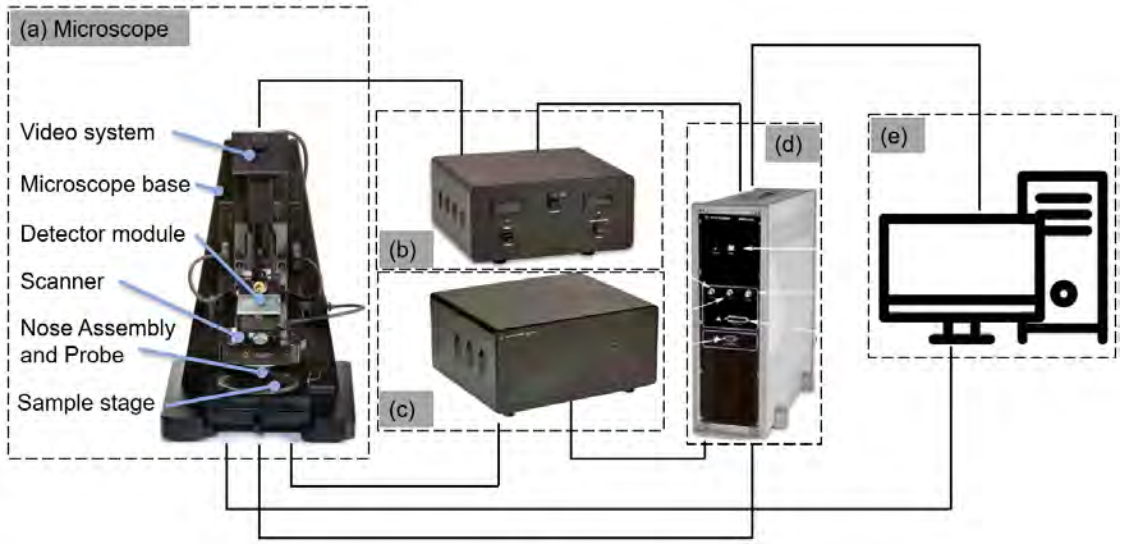

Figure 3.8: The Agilent 5400 AFM system. The Head Electronics Box (a) is connected to the microscope (b) to provide the power supply of the laser diode and read the signal from the detector. The AFM Controller (d) provides the high voltage to the piezoelectronics and other control functions. The MAC Mode Controller (c) is the hardware for MAC mode. It can also determine the oscillation amplitude more precisely. A computer is connected to the microscope and the AFM Controller to process the measurement. Instrument pictures are taken from the user's guide of the microscope [24].

The main component of the Agilent 5400 AFM system is the microscope as shown in figure 3.8. It includes a magnetic sample stage, a scanner with either a normal AFM tip or a magnetic tip, a laser diode and detector, and a video system to locate the cantilever. The other component is the control system, which includes a Head Electronics Box, a AFM controller, a magnetic AC controller and a computer. In addition, there is an environmental enclosure box to insulate from acoustic and vibrational noise.
Since the AFM images and the MFM images should be acquired simultaneously, a ferromagnetic tip is used for scanning instead of a normal AFM tip. First, the AFM images are taken through an AC-scan, which is also known as the tapping mode, at a position close to the sample surface with similar parameters that were used for a normal AFM. Then, at every scan position of the same area a second measurement is performed at a pull away distance. This measurement detects the changes in resonant frequency and phase of the cantilever that are due to the magnetic force between the sample and the tip.
The cantilever is driven at the corresponding resonant frequency. During the measurement the oscillation of the cantilever is measured by a laser system through a

4-quadrant detector as shown in figure 3.9(a). For the AFM measurement, the change of the amplitude caused by the interaction between sample surface and tip is compensated by a height correction of the scanner by a piezoelectric component, which produces the topological height profile. For the MFM measurement as shown in figure 3.9(b), the phase of the oscillation is changed by the magnetic force between the magnetized tip and magnetic sample, so that the MFM images could be used to analyze the magnetic domain structure.

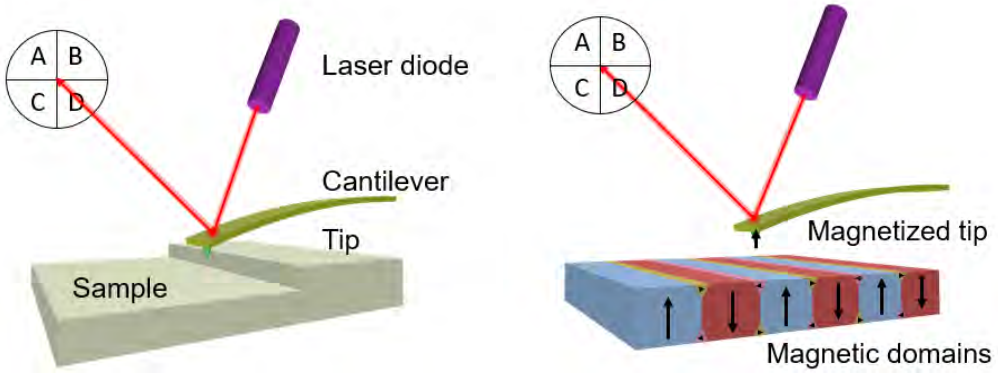

(a) Principle of the AFM (b) Principle of the MFM

Figure 3.9: The Agilent 5400 AFM system.

3.2.4 Magnetic Property Measurement System

A Magnetic Property Measurement System (MPMS) from Quantum Design has been used for measuring the magnetic properties of samples. The main component of the system is the probe cylinder inside the dewar tank as shown in figure 3.10, which includes a sample rod for loading samples, a sample transport for automatic sample measurements and position calibration, a superconducting solenoid to generate reversible magnetic fields up to +/- 7 Tesla, and a SQUID detector system with a magnetic shield to measure the magnetization of samples precisely.

Since the SQUID is extremely sensitive to magnetic field, and in order to avoid the effects from the surrounding magnet, the SQUID does not measure the magnetization of the sample directly. Instead, as shown in figure 3.10, the sample moves through a superconducting coil (also called pick-up coil [25]), which is connected to the SQUID system that is installed in a magnetic shield. The shield provides a volume of extremely stable magnetic field to protect the sensitive sensor from fluctuations from the environment. The measurement in the MPMS system is performed by moving the sample through the superconducting detection coil, which is built as a second order gradiometer. The superconducting wire goes first one circle counter-clockwise, two circles clockwise and then one circle counter-clockwise again. This method is used to reduce noise in the detection circuit caused by fluctuations in the large magnetic field of the superconducting magnet [26]. The superconducting detection coil measures the local changes in magnetic flux density produced by the movement of the sample. The SQUID electronics, therefore,

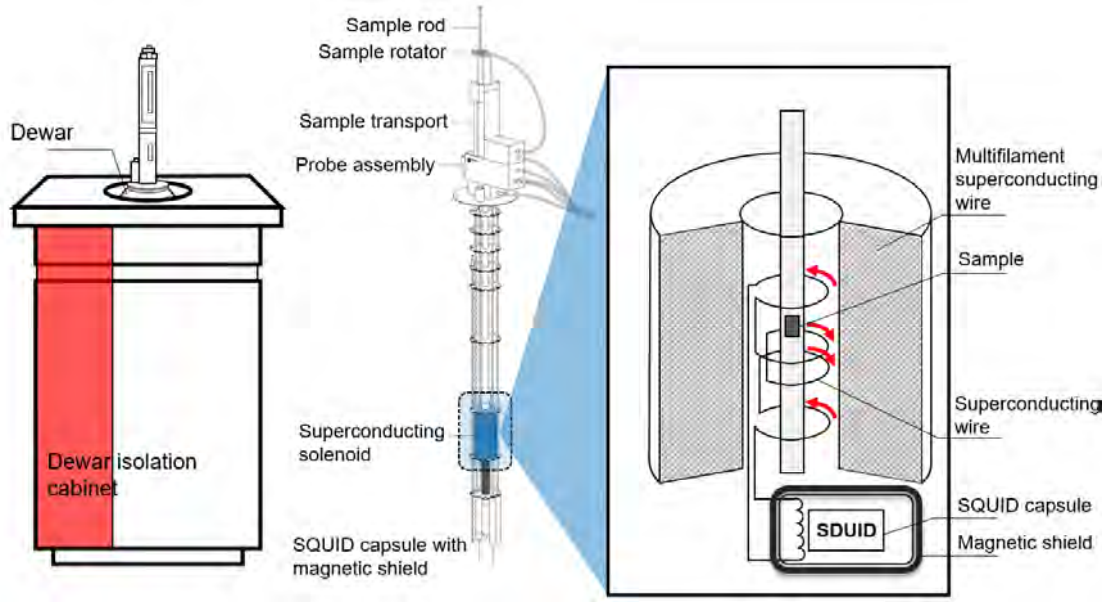

Figure 3.10: The MPMS system. The probe cylinder was installed in a dewar that is protected by a isolation cabinet. The sample was loaded inside a superconducting solenoid that produces high field. The magnetization of samples were detected by a superconducting coil and measured by a SQUID system with a magnetic shield. The sketches are inspired from the user's manual.

produces a output voltage that is proportional to the magnetization of samples.
The MPMS system has a direct current (DC) option and a reciprocating sample option (RSO). In DC mode the sample moves through the superconducting coil with discrete steps. By using the RSO option the sample can oscillate rapidly through the superconducting coil. Therefore, the RSO option is faster and more accurate (5×10^{-9}emu) than the DC option [25].

3.2.5 Physical Property Measurement System

A physical property measurement system (PPMS) from Quantum Design has been used to measure the electrical transport properties of samples in this project with a maximum applied magnetic field up to +/- 9 Tesla and temperatures between 1.9 and 400 K.

As shown in figure 3.11, the basis of the system is a dewar containing liquid helium. The main component for the measurement is the probe that includes a probe head, rods and a sample chamber, where samples were loaded. A large coil is installed around the sample chamber to provide a magnetic field up to 9 Tesla. The very base of the sample space contains a 12-pin connector that contacts the bottom of an installed sample puck. Two thermometers and a heater are installed just below the sample puck connector. The region between the sample space and the thermal insulator is used as a cooling annulus. Helium is pulled through the impedance tube into the cooling annulus through the bellows, so that the sample space can be cooled or warmed during the measurement [28].

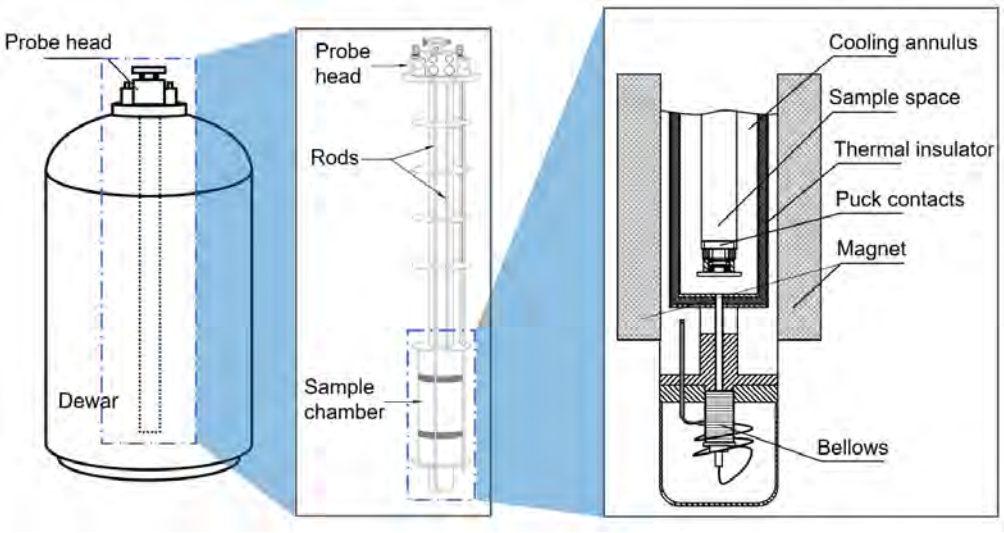

Figure 3.11: The PPMS system. The probe cylinder was installed in a dewar. The sample was loaded inside the sample space surrounding by a superconducting solenoid that produces high field. The transport properties of samples were measured through a puck with corresponding electric contacts. The sketches are inspired from the user's manual of the PPMS system.

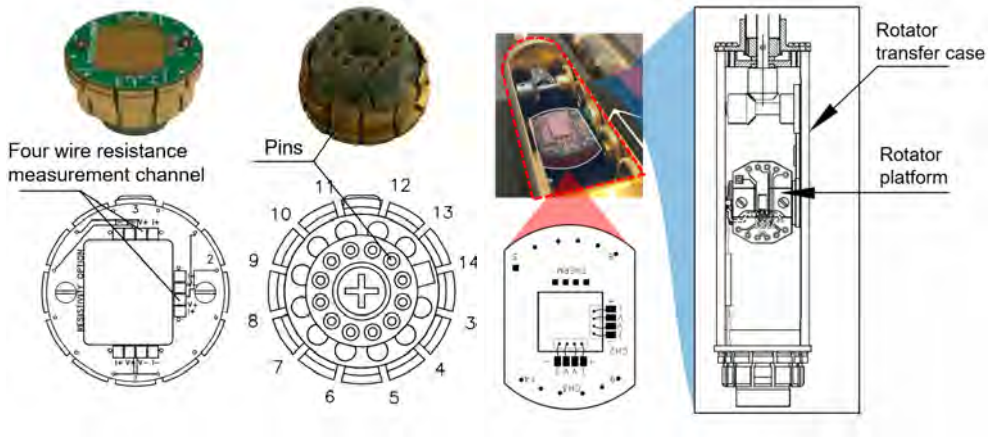

(a) Standard puck for resistivity measurements.

(b) Horizontal rotator probe for resistivity measurements.

Figure 3.12: Pictures and schematic sketches of a standard PPMS puck (a) and a horizontal rotator probe (b) for resistivity measurements. There are three channels available to perform four-wire resistance measurements and 12 pins to connect to the sample chamber on a standard resistivity puck(a). There is a rotatable platform with a sample holder board in a horizontal rotator probe(b) [27]. The sample holder board has two channels for four-wire resistance measurements.

Samples were mounted on a standard resistivity sample puck to perform a magneto-resistivity measurement as shown in figure 3.12(a). There are three channels available and each channel has four contacts, one positive and negative contact for current and voltage, so that the PPMS system may measure up to three samples at one time [29]. In order to measure the magneto-resistance with in-plane applied magnetic field, a horizontal rotator probe is needed to mount the sample parallel to the magnetic field. As shown in figure 3.12(b), the sample holder board was installed on a rotator platform and can be rotated around a horizontal axis. The board has 2 channels available, so that the PPMS system can measure the magneto-resistances that are parallel and perpendicular to the applied field.

4 Result and Discussion

The samples under investigation were grown by the oxide molecular beam epitaxy (OMBE) system at JCNS-2 using different growth methods. For the thin film system, many physical properties are related to the magnetic domain structure, e.g. the component of the closure domains determines the in-plane magnetization and the domain wall structure determines the resistivity. Therefore, the domain structure can be studied by measuring and analyzing these physical properties.

4.1 Sample Preparation

One of the most important advantages of the OMBE technique is the possibility to grow perfectly epitaxial thin films. There are many parameters that control the thin film growth such as growth temperature, growth rate and growth methods. The optimized parameters for tunable perpendicular magnetic anisotropy (PMA) have been determined by Annika Stellhorn [14]. Although the layer stacks in this project are slightly different, we can start with these optimized growth parameters to prepare our samples.

4.1.1 Substrate Preparation

The substrates which are used in this project are one-side epi polished MgO substrates from CrysTec GmbH with lattice constant $a = 0.4212\,\text{nm}$ [30]. In order to generate a clean and smooth surface on the substrate for growing crystalline thin film epitaxially, the substrate was blown by a nitrogen flow to remove the dust and annealed at 450 °C for 1 hour then 550 °C for 10 minutes in the main chamber of the OMBE system in vacuum down to 10^{-11} torr.
The effect of the annealing on the surface state can be characterized by comparing the RHEED images as shown in figure 4.1.

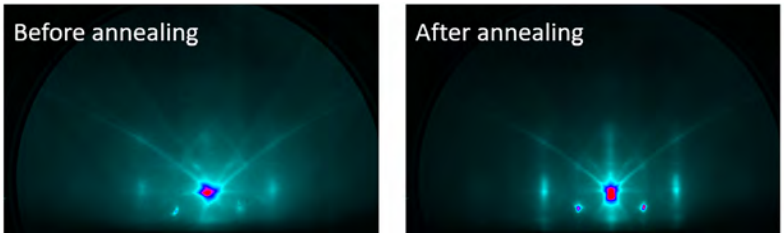

Figure 4.1: The RHEED pattern before and after annealing. Both patterns were taken in the [110] orientation

The RHEED pattern before annealing is slightly blurred compared to post-annealing. This indicates the annealing process reduced the surface roughness. The RHEED pattern after annealing shows streaks, which means the MgO substrate has a flat surface with small domains. Furthermore, both RHEED pattern have clear Kikuchi lines, which indicate the single-crystalline property of the MgO substrate.

4.1.2 Determination of the Growth Parameters

In order to grow a stoichiometric crystalline thin film with proper thickness, the optimized parameters including growth temperature, growth rate and thickness were taken from previous work done by Annika Stellhorn. The growth rate was monitored by a quartz microbalance and the rate was mainly determined by the temperature of the effusion cell. The resonant frequency of the quartz changes with the mass of materials deposited on its surface

$$T = Ct\frac{\partial f}{\partial t} \tag{4.1}$$

where T is the thin film thickness, C is a constant, t is the growth time and $\frac{\partial f}{\partial t}$ is the change rate of the resonant frequency. Since it is almost impossible to exactly adjust $\frac{\partial f}{\partial t}$ to a stable value that is the same as the optimized value, the growth time of both Fe and Pd should be corrected individually by

$$t_{Pd} = t_{Pd,ex}\frac{\frac{\partial f}{\partial t}_{Pd,ex}}{\frac{\partial f}{\partial t}_{Pd}} \tag{4.2}$$

and

$$t_{Fe} = t_{Fe,ex}\frac{\frac{\partial f}{\partial t}_{Fe,ex}}{\frac{\partial f}{\partial t}_{Fe}} \tag{4.3}$$

where $t_{Pd,ex}$, $t_{Fe,ex}$, $\frac{\partial f}{\partial t}_{Pd,ex}$ and $\frac{\partial f}{\partial t}_{Fe,ex}$ are optimized parameters.

4.1.3 Thin Film Growth

As planned, two samples with different PMA were prepared using co-deposition and shuttered growth methods to grow the FePd layer. Co-deposition is a process where two materials are deposited on a surface simultaneously. Shuttered growth means two or more effusion cell sources are controlled by opening and closing shutters so that different materials can grow monolayer by monolayer.
The growth process is schematically shown in figure 4.2. A Pd buffer layer was grown on the substrate with flat surface that was prepared by annealing first to reduce the lattice mismatch between the FePd layer and the MgO substrate. This Pd buffer layer was then annealed at 350 °C for 30 minutes to provide a smooth and single crystalline surface. After that, a magnetic FePd layer was grown on the annealed Pd buffer layer by co-deposition or shuttered growth and finally a Pd capping layer was grown on the top to prevent the oxidation of the FePd. The detailed summary of growth parameters are listed in table 4.1.

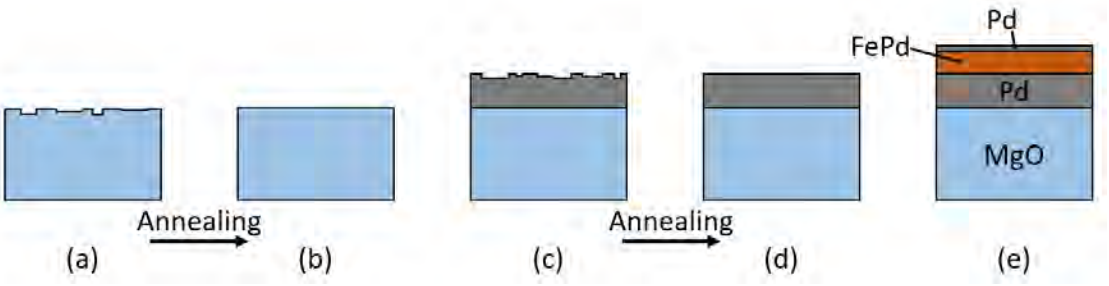

Figure 4.2: (a) Untreated MgO substrate. (b) Annealed MgO substrate. (c) Pd buffer layer before annealing. (d) Pd buffer layer after annealing. (e) The final sample system with a Pd capping layer.

Table 4.1: Optimized growth parameters used for co-deposition and shuttered growth.

SN.	Pd buffer layer			FePd layer				Pd capping layer		
	$\frac{\partial f}{\partial t}$ [Hz/s]	t [s]	T [°C]	$\frac{\partial f}{\partial t\ Pd}$ [Hz/s]	$\frac{\partial f}{\partial t\ Fe}$ [Hz/s]	t [s]	T [°C]	$\frac{\partial f}{\partial t}$ [Hz/s]	t [s]	T [°C]
0659	-0.864	7600	20	-0.666	-0.314	4830	230	-0.666	370	20
0663	-0.830	7900	20	-0.92	-0.49	4400	230	-0.92	260	20

4.1.4 Low Energy Electron Diffraction

A main factor that affects the magnetic property of the thin film system is the crystalline structure. Besides ex-situ x-ray diffraction, there are two techniques, LEED and in-situ RHEED, installed in the OMBE system that can be used to analyze the crystalline structure just after or during the thin film growth. The LEED is very sensitive to the surface quality and crystalline structure. Additionally, it is possible to calculate the lattice constant of sample surface from LEED patterns if the LEED system was calibrated correctly. Figure 4.3(a) shows a series of LEED patterns that was taken at different electron energy for the sample 0659 after deposition of the final Pd capping layer, and transferring the sample into the buffer line of the MBE system. The distance of the Bragg spots d and the corresponding accelerating voltage U has a relationship given by

$$\frac{1}{d} = \frac{a\sqrt{2m_e e}}{hR}\sqrt{U} \tag{4.4}$$

where a is the in-plane lattice constant, m_e is the electron mass, e is the elementry charge, h is the Plank constant and R is the screen radius. The lattice constant a is calculated from the slope $s = \frac{a\sqrt{2m_e e}}{hR}$ of the linear fit for $\frac{1}{d}$ against $\sqrt{U}$ as shown in figure 4.3(b), which means

$$a = \frac{shR}{\sqrt{2m_e e}} \tag{4.5}$$

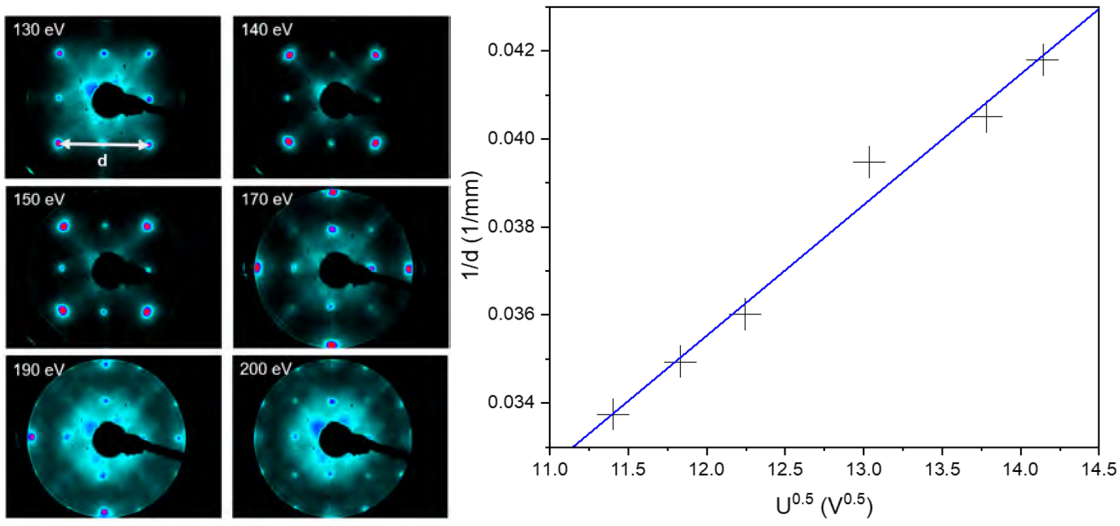

(a) (b)

Figure 4.3: (a) A series of LEED patterns taken at different electron energy. The distance d is defined as shown in the pattern with 130 eV. (b) $\frac{1}{d}$ was plotted against $\sqrt{U}$ and fitted linearly to calculate the lattice constant.

For the sample 0659 as an example, the slope s of the linear fit of $\frac{1}{d}$ against $\sqrt{U}$ is equal to 0.00297±0.0002 $\frac{1}{mm\sqrt{V}}$. The calibrated value of the screen radius R is equal to 73 mm, which leads to the lattice constant a = 3.94±0.26 Å. There is a systematic error which occurs when measuring the distance, because the Bragg spots have a certain extension, which leads to a significant error in the result of the lattice constant.

4.1.5 Reflection High-Energy Electron Diffraction

In-situ RHEED was also performed to track the surface state during the sample growth. Figure 4.4 shows the RHEED patterns during the growth of the sample 0659, grown under conditions which lead to high PMA.

The sharp RHEED spots and Kikuchi lines in figure 4.4(a) indicate that the MgO substrate has a very smooth surface with high crystalline order after annealing. In contrast, just after growth the RHEED pattern of the Pd buffer layer in figure 4.4(b) has broader modulated streaks and the Kikuchi lines are smeared out, which is because the roughness of the Pd buffer layer surface is higher and the film has some out-of-plane magnetization domains whose size is smaller than the coherence length of the electron beams with energy of 15 keV. The RHEED pattern of the Pd buffer layer shown in figure 4.4(c) after annealing shows elliptical streaks and the Kikuchi lines appear again, which indicate that the annealing process flattens the surface and enhances the crystalline order. The RHEED pattern after the growth of FePd and Pd capping layer is also the case as shown in figure4.4(d).

Figure 4.5 shows RHEED patterns that were taken during the growth of the sample 0663, which is grown under conditions leading to low PMA. The RHEED pattern of annealed

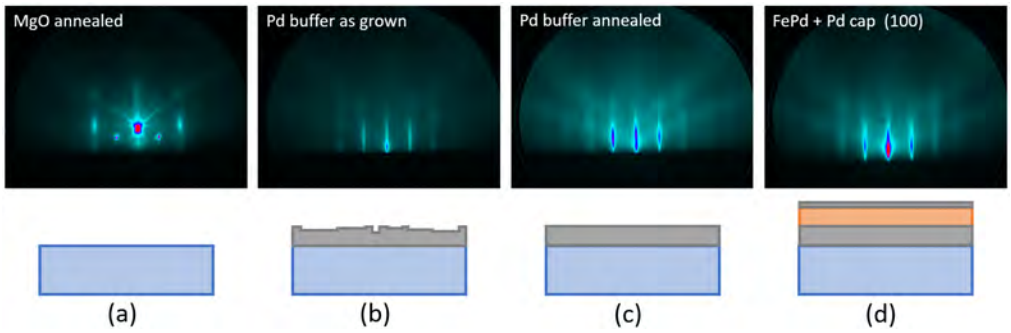

Figure 4.4: RHEED patterns of sample 0659 with high PMA. (a) Annealed MgO substrate with flat surface and high crystalline order. (b) RHEED pattern taken after the growth of Pd buffer layer. The modulated streaks and smeared-out Kikuchi lines indicate the rough surface and out-of-plane domains. (c) (d) Patterns of annealed Pd buffer layer and Pd capping layer. Elliptical streaks and Kikuchi lines denote that the grown film has a flat surface and crystalline structure.

MgO substrate in figure 4.5(a) also has sharp spots and Kikuchi lines because of the flat surface and crystalline structure. Interesting is the RHEED pattern in figure 4.5(b) that was taken after 20 s growth of the Pd buffer layer. The pattern shows bulk-like three dimensional reciprocal points, which indicates that the growth of the Pd buffer layer was started with island growth, so that the glancing electrons are transmitted through the three dimensional islands and produce a transmission diffraction pattern. The RHEED patterns of annealed Pd buffer layer and Pd capping layer could also be explained just like the sample 0659.

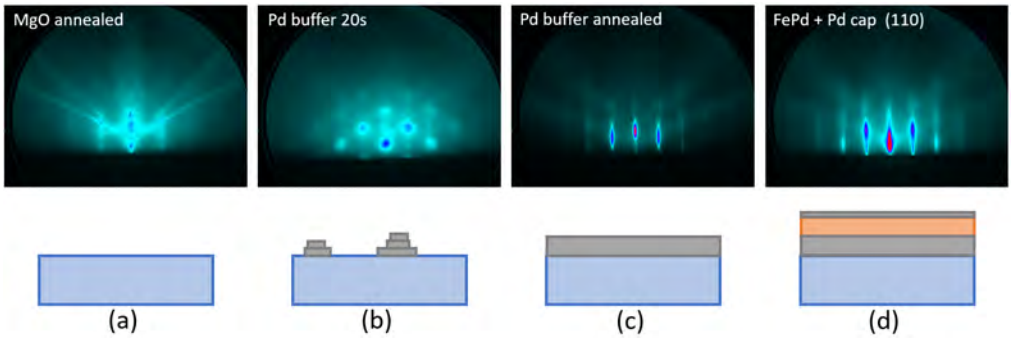

Figure 4.5: RHEED patterns of sample 0663 with low PMA. (a) Annealed MgO substrate with flat substrate and high crystalline order. (b) RHEED pattern of three dimensional reciprocal points indicates the island growth in the beginning of growing Pd buffer layer. (c) (d) Patterns of annealed Pd buffer layer and Pd capping layer. Elliptical streaks and Kikuchi lines denote that the grown film has a flat surface and crystalline structure.

RHEED is also a useful technique for monitoring the structure of grown layers because intensities of diffraction spots show an oscillatory behavior which is directly related to

the layer-by-layer growth process [31]. As shown in figure 4.6 and 4.7, the intensity of one spot in the RHEED pattern is oscillating during the growth of the FePd layer.
For the sample 0659 with high PMA, the oscillation shown in figure 4.6 smears out after about 30 cycles, which indicates that the growth method of co-deposition results in layer-by-layer growth in the beginning and then island growth. One cycle of the oscillation corresponds to the growth of one FePd monolayer. From the first few cycles one could determine that the time cost for one FePd monolayer is about 32 s for the sample 0659. Since the growth of FePd takes 4830 s in total, the FePd layer of the sample 065 al is 3.71

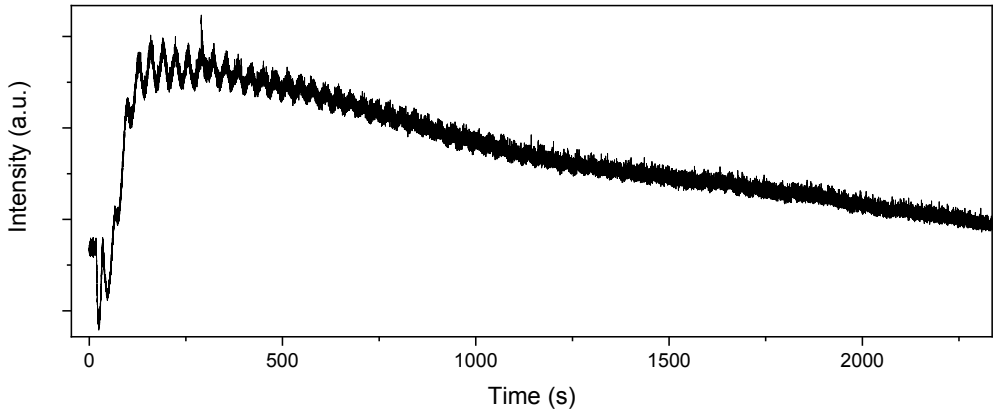

Figure 4.6: The oscillation of one RHEED spot for the sample 0659 during the growth of the FePd layer. The oscillation fades out after about 30 cycles, which means that the co-deposition leads to layer by layer growth only at beginning.

For the sample 0663 with low PMA, the oscillations are present during the whole growth period of the FePd layer as shown in figure 4.7, which means the FePd always grows layer by layer for the shuttered growth. Therefore, the density of crystalline defects in the sample 0663 is much lower than that in the sample 0659. One cycle of the oscillation also corresponds to the growth of one FePd layer. For the sample 0659, the time cost of one monolayer also equals to one cycle of opening and closing of Pd and Fe effusion cells for the shuttered growth. Therefore, the FePd layer of the sample 0663 has 110 FePd monolayers, which corresponds to a thickness of 40.8 nm.

4.2 Characterizations with X-ray

Since the FePd layer with $L1_0$ phase has the highest perpendicular magnetic anisotropy, one could measure the amount of $L1_0$ phase by x-ray diffraction to evaluate the magnetic properties of the samples. In order to characterize the crystal structure, thickness and the interface roughness, x-ray diffraction (XRD) and x-ray reflection (XRR) measurements were performed on a D-8 diffractometer equipped with a copper source that has a wavelength of 1.54 Å. Also, taking advantage of a newly developed in-house technique,

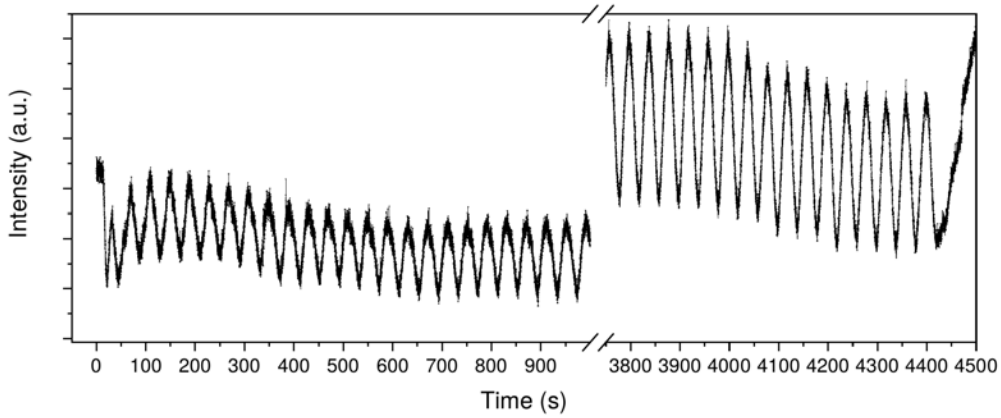

Figure 4.7: RHEED oscillation of the sample 0663. The oscillation lasts until the end of the growth of the FePd layer.

wide-angle x-ray scattering (WAXS) measurements were performed on the GALAXI instrument to investigate the in-plane crystalline structure.

4.2.1 X-Ray Reflection

Layer thicknesses were determined by fitting the XRR data using the software GenX. Both samples were fitted with the same layer stacks, which contains the Pd buffer layer on the MgO substrate, the magnetic FePd layer and the Pd capping layer on the top. The initial parameters such as layer thickness and roughness were taken from past experiments. The initial layer densities were taken from the ICSD database [32].

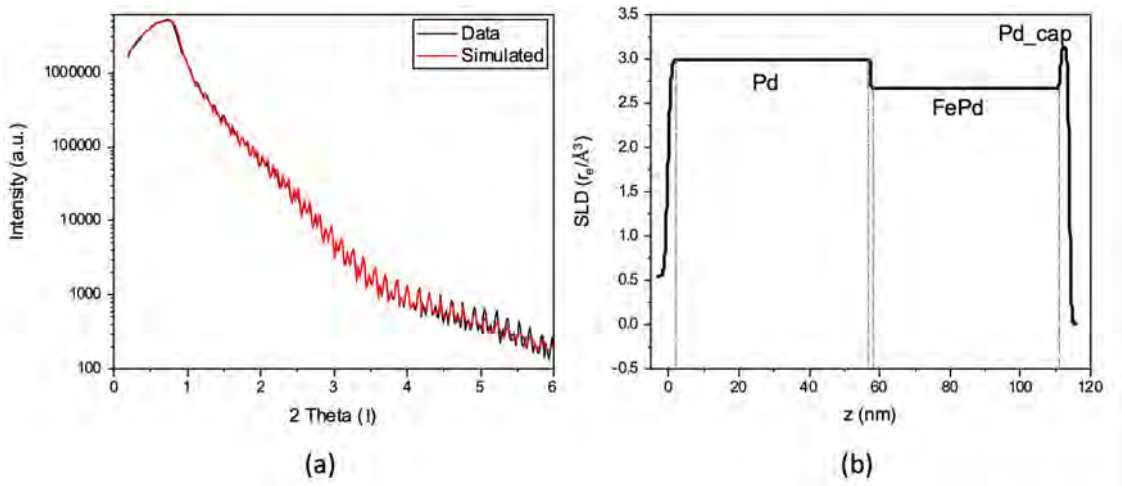

Figure 4.8: (a) X-ray reflectometry measurement of the sample 0659. All the layer thicknesses and densities were obtained via a simulation. (b) The SLD as a function of the height above the substrate.

As shown in figure 4.8(a), the XRR data of sample 0659 can be simulated very well when 2θ is smaller than 4°. The thickness of the FePd layer is 53.9±0.8 nm, which is used

to normalize the magnetization measurement. This thickness has a good agreement with the result from the calculation of the RHEED oscillation (56 nm) in subsection 4.1.4. The simulated scattering length density (SLD) is shown in figure 4.8(b). The SLD value of Pd capping layer is slightly bigger than the of Pd buffer layers because the Pd capping layer is under compressive strain and on the other hand the Pd buffer layer is under tensile strain.
As shown in figure 4.9(a), the XRR data of sample 0663 was roughly simulated. The thickness of the FePd layer for this sample is 35.7±4 nm, which is thinner than the result from the RHEED oscillation (40.8 nm). The most probable reason is that the XRR data can not be fitted perfectly. Note that the SLD value of the Pd capping layer is much lower than expected, which is most likely because the capping layer was already oxidized. What needs to be mentioned is that the XRR is a modeling measurement method and all parameters were given based on the principle of minimizing the error of the simulation results.

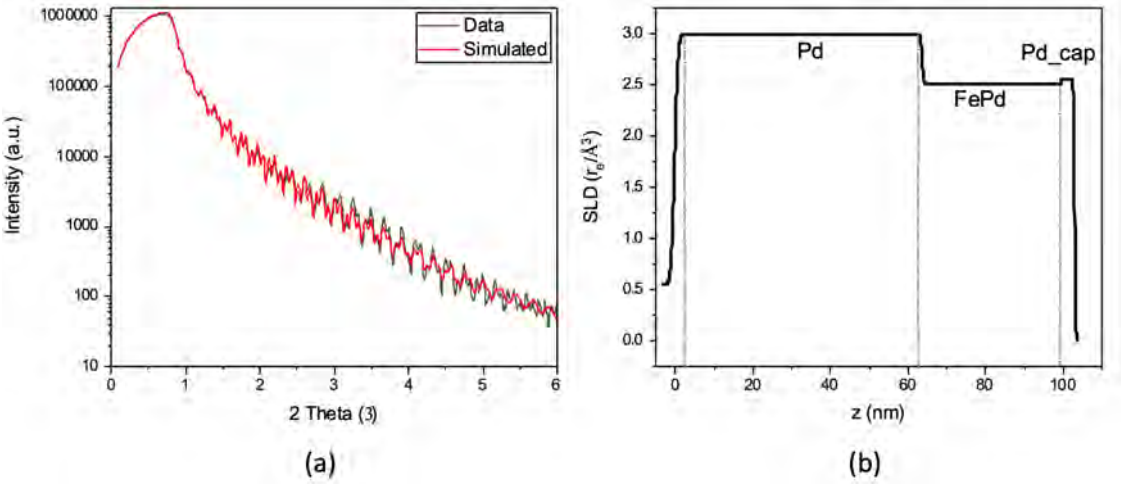

Figure 4.9: (a) X-ray reflectometry measurement of the sample 0663. The XRR data could only be simulated roughly. (b) The SLD as a function of the height above the substrate.

The layer densities of both samples and the corresponding bulk densities from the ICSD database are listed in table 4.2. For the Pd buffer layer, both samples exhibit a smaller value than the bulk density, because the Pd buffer layer was under tensile strain since the lattice constant of Pd is smaller than the MgO substrate's. For the FePd layer, because the lattice was also under tensile strain, the layer density should be smaller than the bulk value, which is the case of the sample 0663. For the sample 0659, the composition of the crystal also plays a very important role here, because it is possible that the film has a composition Fe_xPd_y with y>x, so that the layer density of FePd is higher than the bulk value. However, as mentioned before, one should always remember that the XRR is only a modeling measurement and it is not completely accurate.

Table 4.2: Density values of the sample 0659

Density values [FU/Å^3]	Pd_buffer	FePd	Pd_capping
Bulk value	0.06795	0.03634	0.06795
Fitted value(0659)	0.06477±0.0015	0.03750±0.00073	0.06796±0.00064
Fitted value(0663)	0.06502±0.00244	0.03528±0.00049	0.05529±0.00105

4.2.2 X-ray Diffraction

The crystal structure and long-range order of samples are determined by x-ray diffraction (XRD) measurements. The measurements were performed on a D-8 diffractometer with the diffraction vector that is always normal to the surface of samples. Therefore, only out-of-plane lattice constants could be measured.

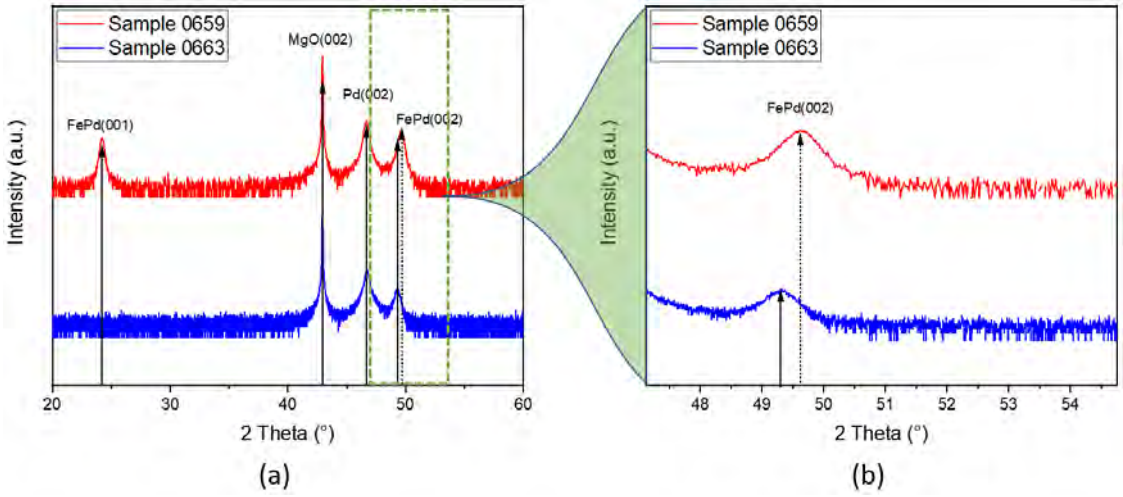

Figure 4.10: (a) X-ray diffraction spectra of both samples. FePd(001) peak disappears for sample 0663. (b) Zoom in of the FePd(002) peak area. The FePd(002) peak of sample 0663 shifts a bit to the left.

The XRD patterns of both samples are shown in figure 4.10(a). Lattice constants of corresponding peaks are calculated as shown in table 4.3. Compared to sample 0659, the FePd(001) peak in the XRD pattern of sample 0663 disappears and the peak of FePd(002) has shifted a bit to the left as can be seen in figure 4.10(b).
The lattice constants $a_{FePd(001)}$ and $a_{FePd(002)}$ of sample 0659 are both smaller than the bulk value of the $L1_0$ phase lattice constant, because the FePd layer is under tensile strain, which decreases the lattice constant in z direction. The tensile strain inside the Pd buffer layer is also the reason why the lattice constants calculated from $a_{Pd(002)}$ peaks of both samples are slightly smaller than the bulk value. Since the lattice constant in z direction of pure $L1_0$ phase FePd is smaller than the lattice constant of a totally random FePd sample, $a_{FePd(002)}$ of sample 0659 is slightly smaller than that of sample 0663, so that the FePd(002) peak of sample 0663 was shifted to the left.
The long-range order parameter S was defined to make it convenient for measuring the

Table 4.3: Lattice constants calculated from the XRD measurement and corresponding bulk values. [11][33]

Lattice constant	$a_{FePd(001)}$ [Å]	$a_{FePd(002)}$ [Å]	$a_{MgO(002)}$ [Å]	$a_{Pd(002)}$ [Å]
Bulk value	3.71	3.71	4.212	3.89
Sample 0659	3.67±0.18	3.67±0.21	4.209±0.096	3.88±0.19
Sample 0663	-	3.69±0.16	4.208±0.085	3.88±0.20

long-range order property of the FePd layer. For the composition of $Fe_{0.5}Pd_{0.5}$, the area of the fundamental peak (002) of the FePd layer $A_{(002)}$ is represented by

$$A_{(002)} = Km(LP)_{(002)}FF^*_{(002)} \tag{4.6}$$

and for a superstructure reflection, the area of peak FePd(001) is given by

$$A_{(001)} = Km(LP)_{(001)}FF^*_{(001)} \tag{4.7}$$

with a constant K, multiplicity m, Lorentz-polarization factor (LP) and the structure factor squared FF^*. The Lorentz-polarization factor (LP) depends on the peak angle θ and the angle α of the monochromator

$$(LP)(\theta) = \frac{1 + cos^2(2\theta)cos^2(2\alpha)}{1 + cos^2(2\alpha)sin(2\theta)} \tag{4.8}$$

The structure factor squared FF^* for the fundamental peak and the superstructure reflection are given by

$$FF^*_{(001)} = 4S[(f_{Fe}e^{-M} - f_{Pd}e^{-M})^2 + (\Delta_{Fe}e^{-M} - \Delta_{Pd}e^{-M})^2] \tag{4.9}$$

and

$$FF^*_{(001)} = 4[(f_{Fe}e^{-M} + f_{Pd}e^{-M})^2 + (\Delta_{Fe}e^{-M} + \Delta_{Pd}e^{-M})^2] \tag{4.10}$$

where S is the long-range order parameter, f_{Fe} f_{Pd} Δ_{Fe} and Δ_{Pd} are the real and imaginary parts of scattering factor for both Fe and Pd sites, M is the Debye-Waller factor, which can be calculated by

$$M = B(\frac{sin(\theta)}{\lambda})^2 \tag{4.11}$$

The long-range order parameter S is obtained from equation 4.6 to 4.7 [34][35]

$$S = \frac{A_{(001)}(LP)_{(002)}[(f_{Fe}e^{-M} + f_{Pd}e^{-M})^2 + (\Delta_{Fe}e^{-M} + \Delta_{Pd}e^{-M})^2]}{A_{(002)}(LP)_{(001)}[(f_{Fe}e^{-M} - f_{Pd}e^{-M})^2 + (\Delta_{Fe}e^{-M} - \Delta_{Pd}e^{-M})^2]} \tag{4.12}$$

Involved parameters are taken from [36] and are listed in table 4.4.

The peak area was determined by using a Gaussian peak fit as shown in figure 4.11 for both samples. Fitted peak areas and peak positions are listed in table 4.5. Therefore, the long-range order parameter could be calculated by using equation 4.12. Results are also shown in table 4.5.

Table 4.4: Parameters that are used to calculate the long-range order parameter S.

Parameters	f_{Fe}	f_{Pd}	Δ_{Fe}	Δ_{Pd}	B_{0659}	B_{0663}
Value	21.05	39.78	3.4	4.2	2.41	3.0

Table 4.5: Experimental parameters that are used to calculate the long-range order parameter S.

Parameters	$A_{001}[a.u.]$	$A_{002}[a.u.]$	$\theta_{001}[°]$	$\theta_{002}[°]$	$\alpha[°]$	S
Sample 0659	53.76±1.37	138.29±9.49	12.10±0.27	24.81±0.39	13.25	0.375
Sample 0663	0	50.93±6.72	-	24.65±0.45	13.25	0

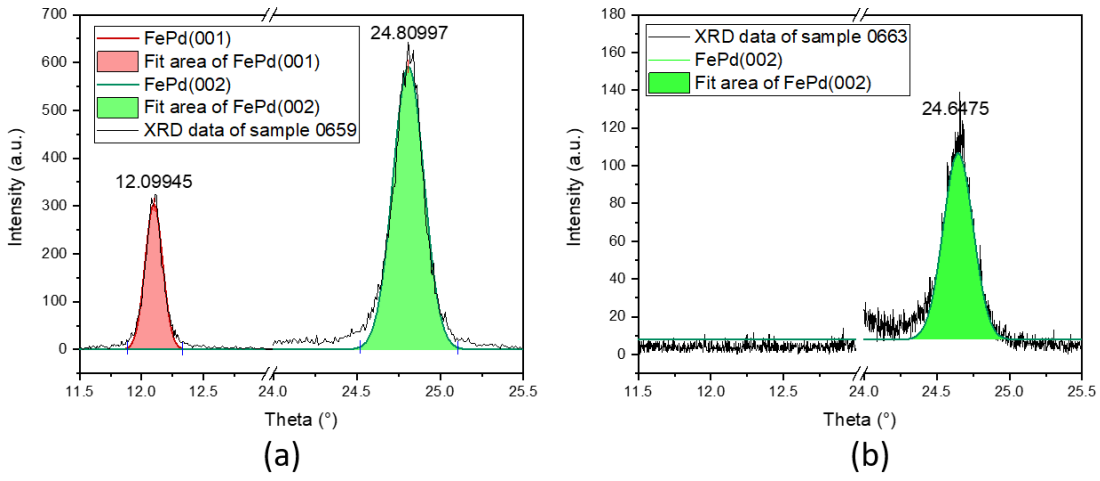

Figure 4.11: (a) Fitted peak and peak areas of both FePd(001) and FePd(002) sample 0659. (b) Fitted peak and area of FePd(002) of sample 0663. The FePd(001) peak vanishes.

4.2.3 Wide-Angle X-ray Scattering

Since the **Q** vectors of XRD measurements performed on the D-8 diffractometer are always normal to the sample surface, only out-of-plane lattice parameters can be measured. As a supplement to characterize the in-plane crystalline structure, the wide-angle x-ray scattering measurement was performed on both samples by using the instrument installed on the GALAXI platform to investigate the in-plane crystalline structure.
As shown in figure 4.12, the reciprocal space was plotted based on acquired data that has been aligned to the strongest MgO(002) signal. Similar to the XRD data, the FePd(001) peak is only present in the sample 0659 with high PMA as can be seen in figure 4.12(a), which indicates the long-range order of this sample. As well, for the Pd and FePd layer, peaks of the sample 0659 are broader than peaks of the sample 0663, which means that the sample 0663 has better crystalline structure.
What is more interesting is that the individual FePd(-200) peak is not visible in both measurements, which is evidence of the epitaxial growth of the FePd layer, because the FePd and Pd layer have the same in-plane lattice constant so that both peaks have overlapped with each other.

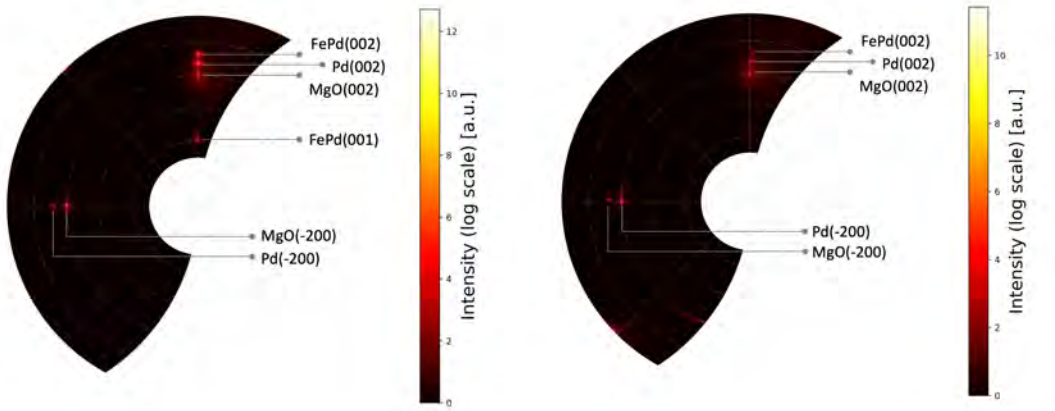

(a) (b)

Figure 4.12: Wide-angle x-ray scattering images of the sample 0659 (a) and the sample 0663 (b). The FePd(001) peak is only present in sample 0659. Peaks of the sample 0659 are broader than the sample 0663. The in-plane FePd(-200) peak has overlapped with the Pd(-200) peak.

4.3 Surface and magnetic domain characterization

An atomic force microscopy (AFM) equipped with a magnetized tip was operated in magnetic force microscopy (MFM) mode, so that normal AFM images and MFM images that contain the information of out-of-plane magnetic domain structures could be obtained simultaneously.

4.3.1 Atomic Force Microscopy and Magnetic Force Microscopy

As shown in figure 4.13(a), the surface of sample 0659 has a lot of terrace structure in two directions that are perpendicular to each other. The exist of the terrace steps might be explained by the plane defect in FePd layer along the (111) crystalline direction [37].

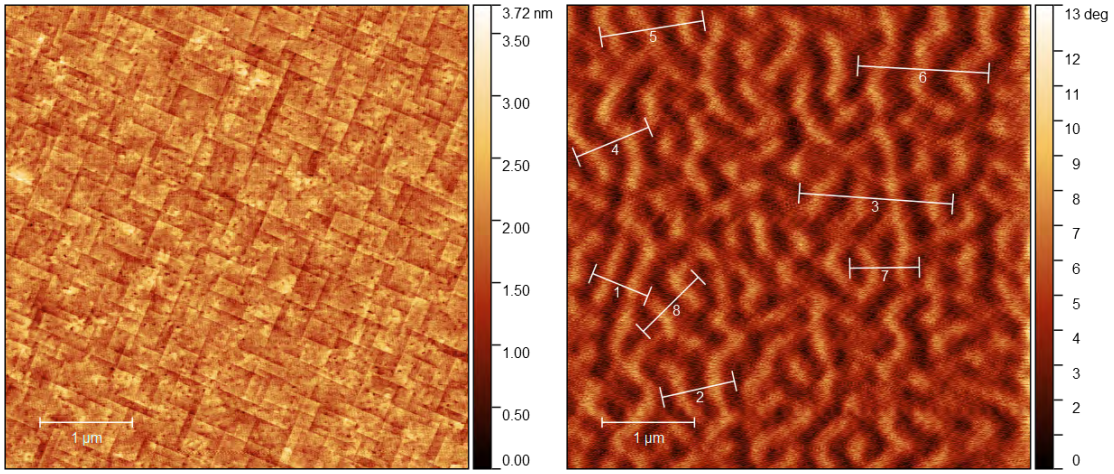

(a) (b)

Figure 4.13: (a) AFM image of the sample 0659. The terrace structure on the surface indicates the existence of plane defects inside the FePd layer. (b) A maze MFM image of the sample 0659. Several profiles were extracted to measure the width of domains.

These terrace features correspond to the microtwins, which relax the strain in the FePd layer induced by the lattice misfit between the FePd layer and the Pd buffer layer (bulk lattice constants for both materials can be found in table 4.3). Dislocations in the FePd layer glide along {111} crystalline planes to reduce the stacking fault energy and form steps that are parallel to <110> direction as can be seen in figure 4.14.

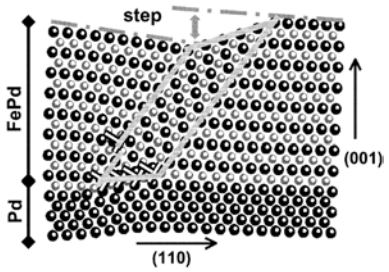

Figure 4.14: Dislocations in FePd film that are parallel to the sample surface glide along {111} crystalline planes to form steps on the surface. the sketch is taken from [37].

Figure 4.13(b) shows the MFM image with irregular maze magnetic domain pattern of sample 0659, which has high percentage of perpendicular magnetic anisotropy (PMA).

The contrast of MFM image originates from the phase shift in the cantilever oscillation during the AC-scan. Dark and bright areas correspond to up and down perpendicular magnetized domains [5]. Therefore, it is possible to determine the domain width through profiles across domains in the MFM image. As shown in figure 4.15, eight profiles were taken at different positions, where at least two parallel bright domains can be found, to reduce the error.

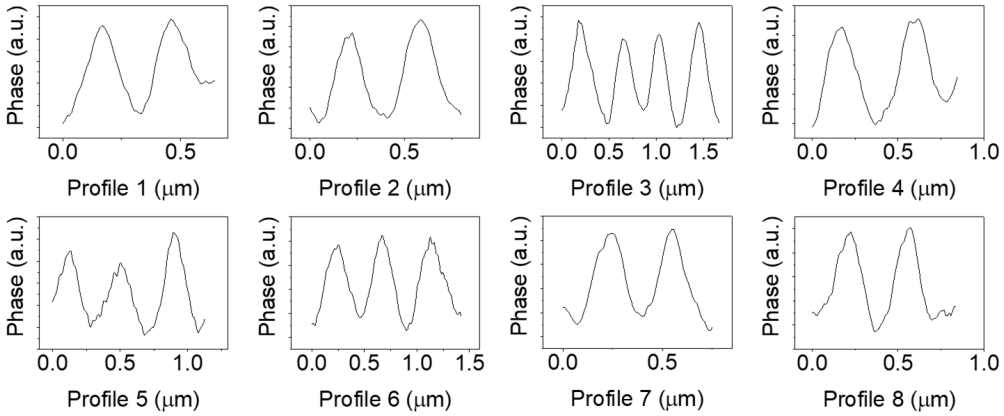

Figure 4.15: 8 Profiles that were taken from the MFM image of sample 0659. The half value of the distance between two peaks is equal to the width of domains.

The AFM image and corresponding MFM image of sample 0663 are shown in figure 4.16. On the sample surface, there are a lot of unavoidable particles, which have a size of 0.3 μm in diameter and 9 nm in height. Since we performed the surface characterization just after the growth, it is not likely that these particles are oxidation island, but probably particles falling from inside somewhere in the OMBE chamber. However, apart of those particles, there is no terrace steps on the sample surface.

The sample 0663 with low percentage of perpendicular magnetic anisotropy exhibits striped magnetic domain pattern in the MFM image. The domain width can be determined by extracting profiles perpendicular to the domain pattern as shown in figure 4.16(b).

4.3.2 Domain Width and A Model of Domain Structure

From profiles in figure 4.15 and figure 4.17 the domain width for both sample can be calculated as shown in table 4.6.

Table 4.6: Domain width of both samples.

Sample number	Domain width [nm]	Error [nm]
0659 (Co-deposited)	186.5	28
0663 (Shuttered)	86.3	6.1

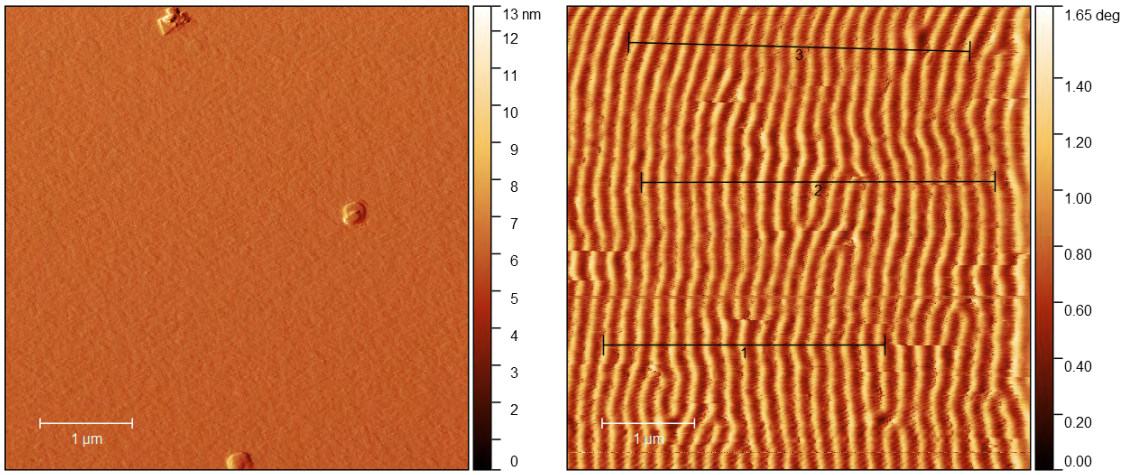

(a) (b)

Figure 4.16: (a) The AFM image of sample 0663. The surface was contaminated with some particles and there is no terrace structure. (b) The strip MFM image of sample 0663. Three long profiles were taken to calculate the domain width.

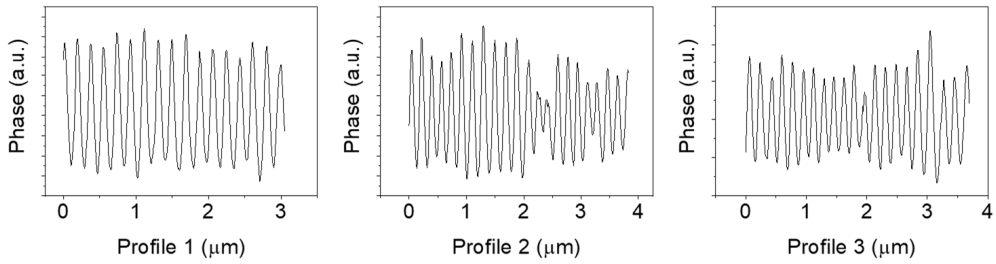

Figure 4.17: 3 profiles that were extracted from the striped MFM image of sample 0663. The half value of the distance between two peaks is equal to the width of domains.

Combined with the thickness that is determined by the XRR measurement, two simplified models of the domain structure can be built as shown in figure 4.18

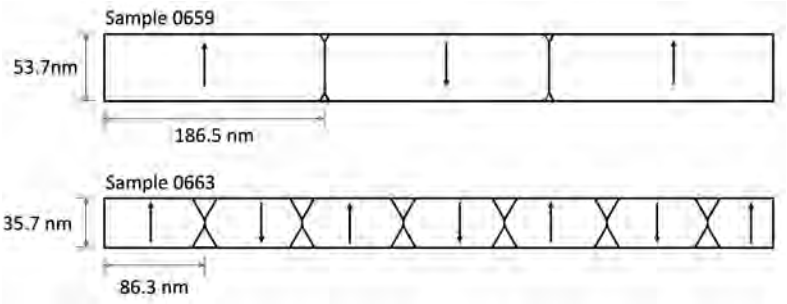

Figure 4.18: Schematic figure of simplified domain structure of both samples. The sample 0659 has more out-of-plane magnetization because of the high S-parameter.

4.3.3 Orientation of the Striped Domain Pattern

As shown in figure 4.16(b), the sample 0663 always exhibits parallel stripe domain patterns in MFM imaging just after the growth to lower the magnetostatic energy [38] because of the presence of the in-plane component of the magnetization. The orientation of stripes was either parallel to (100) direction or (010) direction.

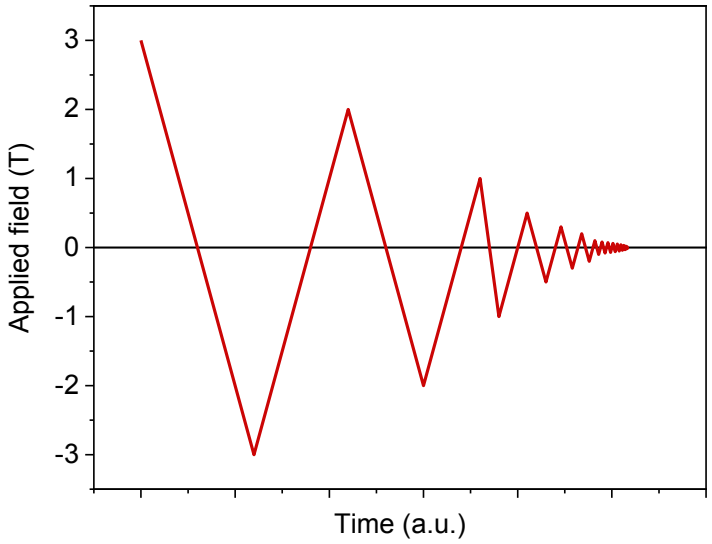

Figure 4.19: The oscillated magnetic field that was applied to demagnetize the sample with low PMA.

The preferred orientation of the parallel stripes depends on the applied magnetic field. Applying an in-plane oscillated demagnetization field as shown in figure 4.19 results in the realignment of the stripe domain patterns to the direction of the applied field. An example experiment can be seen in figure 4.20. The parallel stripe domain

patterns of the shuttered sample 0663 with low PMA were aligned to the vertical applied demagnetization field direction. After that, applying a horizontal demagnetization field realigns the vertical patterns in figure 4.20(a) to horizontal patterns in figure 4.20(b)

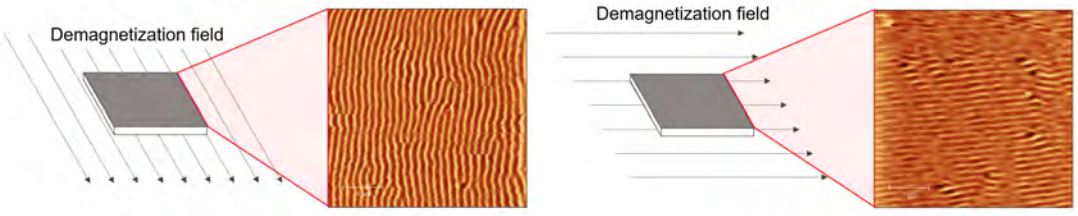

(a) The parallel domain pattern is aligned to the direction of the applied demagnetization field.

(b) The domain pattern of the same sample is rotated for 90 ° by applying a demagnetization field that is perpendicular to the previous field.

Figure 4.20: Schematic figure of the rotatable domain pattern

4.4 Magnetization Measurement and Quantitative Perpendicular Magnetic Anisotropy

The SQUID M-H hysteresis loops were taken with magnetic field up to 6 T applied parallel and perpendicular to the sample surface using the MPMS system from Quantum Design.
The M-H hysteresis loops along the easy and hard axis were acquired at room temperature for both samples as shown in figure 4.21 and 4.22. Since coercive fields of in- and out-of-plane are different, the closure area between in- and out-of-plane provides a quantitative method to evaluate the perpendicular magnetic anisotropy (PMA) for both samples.

The uniaxial quality factor W was used to evaluate the strength of the PMA [39]. The W factor is given by

$$W = \frac{K_u}{K_d} \tag{4.13}$$

with first order uniaxial anisotropy constant K_u and the stray field energy coefficient K_d, which is equal to $\frac{1}{2}\mu_0 M_s^2$ [40]. The uniaxial anisotropy energy K_u was obtained by correcting the effective anisotropy K_{eff} from the contribution of the magnetostatic energy $\frac{1}{2}\mu_0 M_s^2$ [41]

$$K_{eff} = K_u - \frac{1}{2}\mu_0 M_s^2 = \int_0^{M_s} (H_{out-of-plane} - H_{in-plane}) dM \tag{4.14}$$

where M_s is the saturation magnetization and the integer is the closure area A between in- and out-of-plane. Therefore, the W factor can be calculated by

$$W = \frac{A}{\frac{1}{2}\mu_0 M_s^2} + 1 \tag{4.15}$$

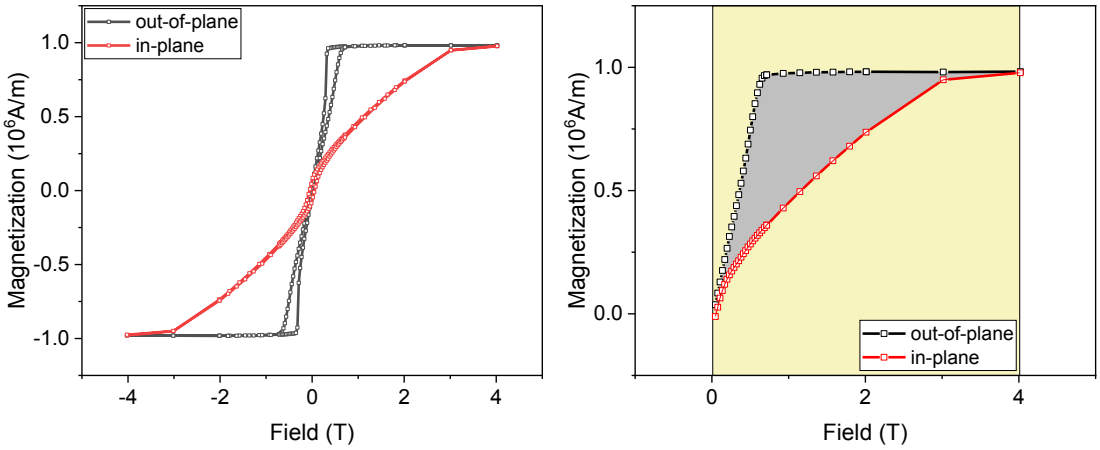

Figure 4.21: In- and out-of-plane M-H hysteresis loops performed on the sample 0659 at room temperature and the closure area between both hysteresis loops.

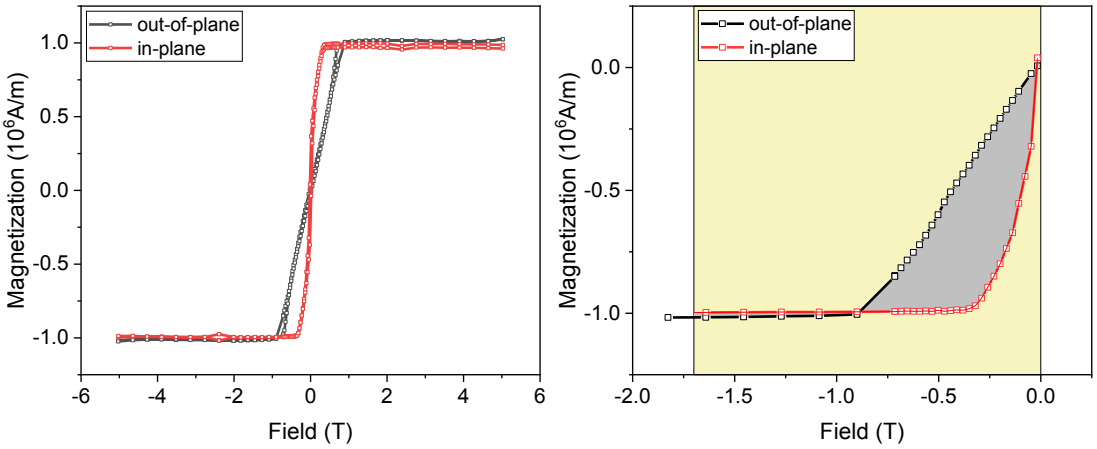

Figure 4.22: In- and out-of-plane M-H hysteresis loops of sample 0663 measured at room temperature. The negative closure area was taken because there is a mismatch in the positive region.

The closure area A was calculated using the integration function in the OriginLab software as can be seen in figure 4.21 and 4.22. The PMA of both samples, therefore, can be evaluated by using the quality W factor, which are listed in table 4.7. The bigger the W factor, the higher the percentage of PMA.

Table 4.7: W factors of both samples. The closure area of sample 0663 is a negative value, because the coercive field of in-plane M-H hysteresis loop is smaller than out-of-plane loop.

Sample No.	A $[10^6 TA/m]$	M_s $[10^6 A/m]$	W
0659	0.922	0.98±0.02	2.528±0.100
0663	-0.298	0.99±0.03	0.506±0.099

4.5 Magnetoresistance and Domain Switching

The result of SQUID M-H measurements indicates that both samples have different percentages of perpendicular magnetic anisotropy. Because the magnetic moments in the thin film tends to form a closure magnetic domain to minimize the magnetostatic energy, one can build simplified models of domain structure for both samples with the help of corresponding MFM images. It was recognized that domain walls in ferromagnets provide additional resistance. This resistance drops significantly by applying a strong magnetic field to saturate the magnetization and erase domain walls [42]. In a magnetoresistance measurement, applied field was oscillated between positive and negative saturation field. The magnetoresistance, therefore, is an indirect method to analyze the domain structure as well as the switching process.

4.5.1 Magnetoresistance Measurements on High PMA Sample

For the sample 0659 with high percentage of perpendicular magnetic anisotropy, two measurements with applying magnetic field parallel or normal to the sample surface were performed in a Quantum Design PPMS system.

Figure 4.23 shows the result of magnetoresistance measurements with applying out-of-plane magnetic field at different temperatures from 200 K to 40 K. There are two regions in the data, the high field resistance background and the domain wall resistance during the switching of magnetization. In the high field region, where the sample was in saturation state, the resistance was affected by several factors such as Lorentz force, magnon suppression and the misalignment of the four-point measurement. The high field magnetoresistance can be fitted to a phenomenological expression

$$\frac{\Delta R}{R_0} = aH^2 + bH + c\,|H| \tag{4.16}$$

where the first term is the contribution of Lorentz force, the second term accounts for Hall effect due to the misalignment of four electrical contacts, the last term is the magnon

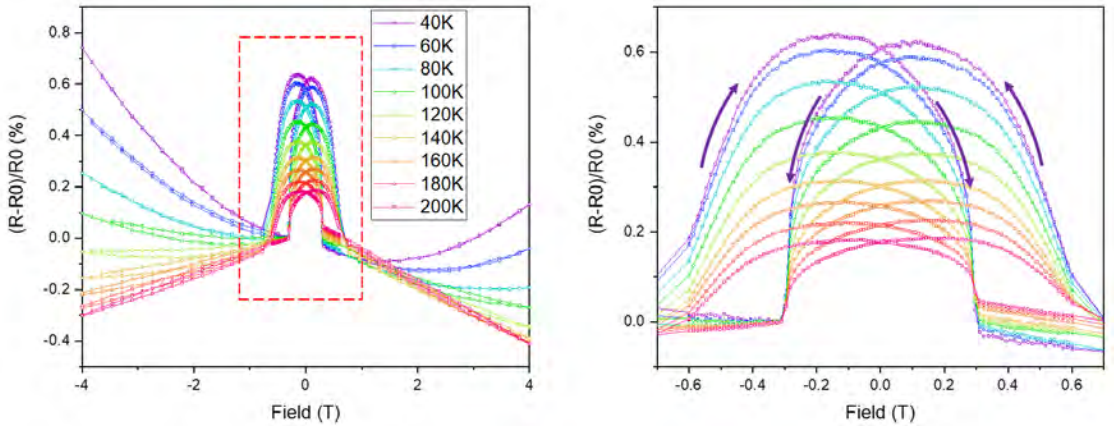

Figure 4.23: Magnetoresistance data of the high PMA sample 0659 recorded at various temperature with applying out-of-plane magnetic field (left). The center region (right) indicates that the domain wall resistance increases with decreasing temperature. The background originates from Lorentz-force and magnon scattering.

suppression contribution [43]. Since the Lorentz force became noticeable especially at low temperature, the shape of the background magnetoresistance slowly changes to a parabolic at low temperature as shown in figure 4.23.

In order to track the switching process of magnetization and gain a more physical understanding of the domain structure, the center domain wall resistance region needs to be discussed in more detail. The magnetization switching process was initialized by nucleation of reversed domains and accomplished by the domain wall motion [44]. With the help of the corresponding out-of-plane M-H hysteresis loop, which was recorded at the same temperature, a switching model was built to explain the magnetoresistance data taken at 40K as shown in figure 4.24.
Applying a negative high field to saturate the sample (Position 1), magnetic moments in the sample are all aligned parallel to the field direction, which means there is no domain wall in the sample. Therefore, the sample was in a relatively low resistance state. With increasing field, a strong enhancement of resistance was observed at position 2. This enhancement in resistance indicates that some domain walls nucleate a small reversed domain is formed. If the field keeps increasing, more and more reversed domains will nucleate and the existing domains will grow through domain wall motion until the domain wall density reaches the maximum at position 3. By further increasing the field, a strong decrease of the resistance is observed because most of the domain walls are destroyed by the domain wall motion towards each other (Position 4). The sample is back to a saturation state without domain walls by increasing the field to saturate the sample (Position 5) [45].

The domain switching mechanism shown in figure 4.24 is a good phenomenological model to explain the switching process and interpret the data of out-of-plane magnetoresistance. Now the magnetic field was applied parallel to the sample surface and the in-plane magnetoresistance data is shown in figure 4.25. The in-plane switching process

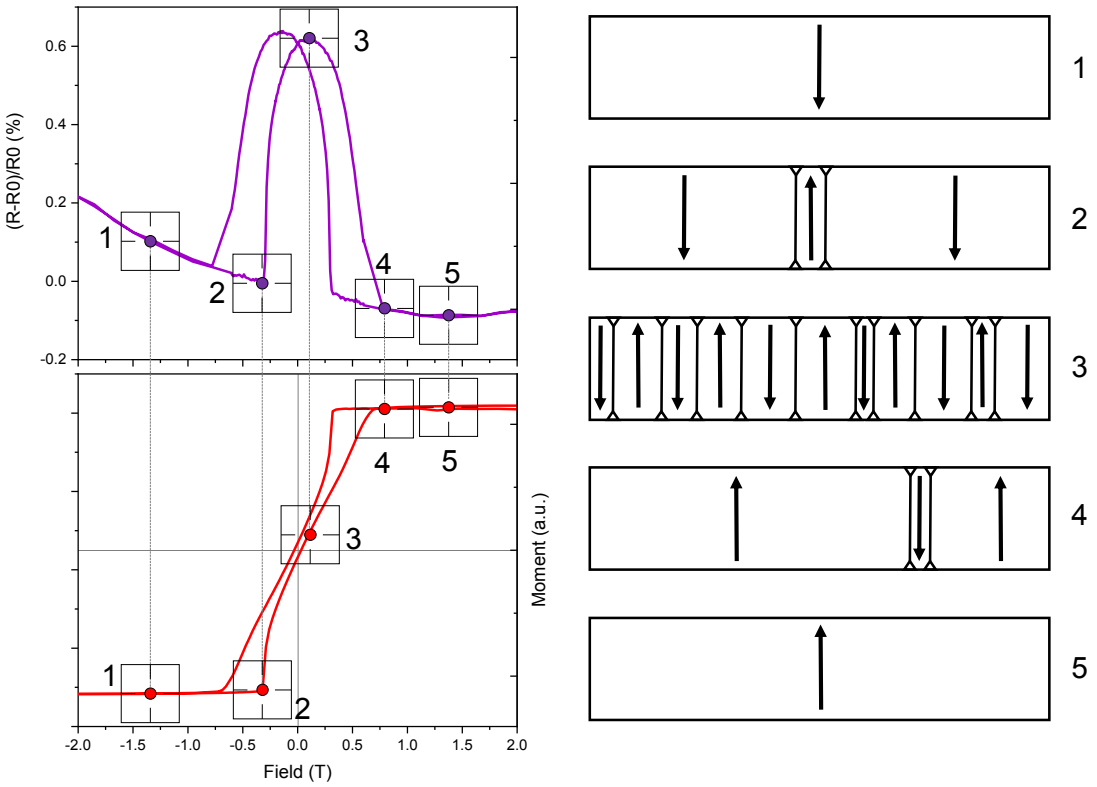

Figure 4.24: The magnetoresistance and corresponding magnetic hysteresis loop of the high PMA sample 0659 recorded at 40 K with applying out-of-plane magnetic field (left). Lateral domain structure at different stages during the magnetization switching (right).

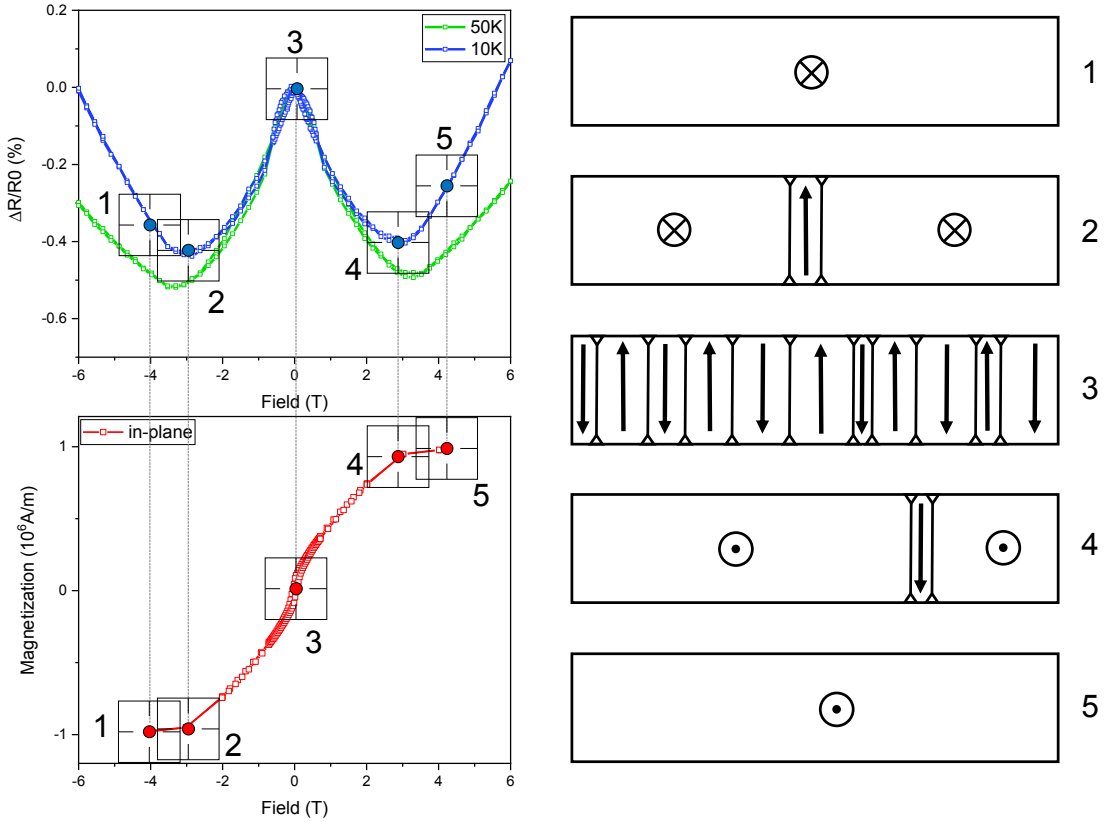

Figure 4.25: The in-plane magnetoresistance and corresponding magnetic hysteresis loop of the sample 0659 (left). Lateral domain structure at different stages during the magnetization switching (right).

can be interpreted by a model with the same domain structure.
The sample is in saturation state without any domain walls if a negative in-plane high field is applied, so that the sample is at relatively low resistance state at position 1. With the decrease of the field, at position 2 magnetic moments of some small domains start to flip to the out-of-plane orientation, which is the direction of the easy axis. As a result, some domain walls are created in the sample and the resistance starts to increase. When the field decreases to around zero at position 3, all the moments are aligned out-of-plane, which is the easy axis for the high PMA sample. Then moments in the sample tend to form a head-to-tail multi-domain structure to minimize the magnetostatic energy and the resistance reaches a maximum. When the field increases further, most of the moments will be aligned to the positive in-plane field direction at position 4. Most of the domain walls will be destroyed and the resistance will decrease back to a low resistance state until the positive saturation state at position 5.
Because of the easy and hard axis behavior, the curve of the in-plane magnetization measurement is smoother and broader than that of the out-of-plane magnetization measurement, which results in the difference between curves of in- and out-of-plane magnetoresistance measurement as shown in figure 4.24 and 4.25. The amplitude of the curve of in-plane magnetoresistance measurement (about 0.4%) is lower than that of out-of-plane magnetoresistance measurement (0.6%), because the domain wall density after out-of-plane demagnetization is higher than that after in-plane demagnetization.

4.5.2 Magnetoresistance Measurements on Low PMA Sample

In contrast to the high PMA sample 0659, the sample 0663 has a non-negligible in-plane component of magnetization. Magnetic moments in the sample tend to form closure domains to minimize the energy. In order to analyze the domain structure and track the switching process, similar measurements with in- and out-of-plane applied field were performed on the sample 0663 with low PMA percentage.

Data of out-of-plane magnetoresistance recorded at different temperatures are plotted in figure 4.26. Compare to the sample 0659, the magnetoresistance of sample 0663 with low PMA on the one hand has a similar background signal that changes with temperature and can be fitted by using equation 4.16, but on the other hand has a different domain wall resistance contribution that is non-hysterical.
Similarly, combining with the corresponding out-of-plane M-H hysteresis loop that was acquired at the same temperature, the switching process of the magnetic domain can be tracked by using a model with the domain structure of low PMA sample as shown in figure 4.27.

The sample has relatively low resistance at position 1, because all moments in the sample are aligned to the negative field direction and there is no domain wall in the sample when a negative high field is applied normal to the sample surface. With the increase of the field, some magnetic moments tend to flip to in-plane to form a small in-plane domain and create some domain walls, because the easy axis is in-plane and so that the energy cost for in-plane flip is relatively low. As a result, the resistance start to increase at position 2. Since at this position, only a small part of the moments flip to in-plane, the magnetization of the sample 0663 does not change much. The

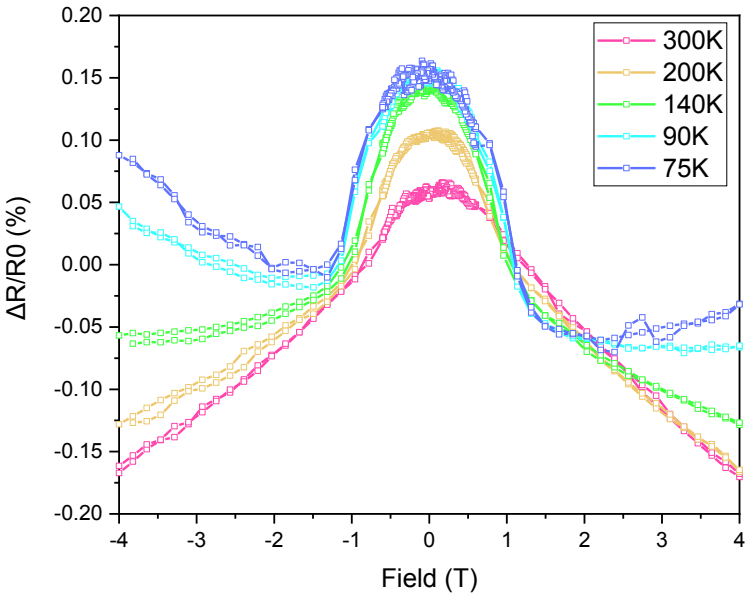

Figure 4.26: Magnetoresistance data of low PMA sample 0663 recorded at various temperature with applying out-of-plane magnetic field. These data have similar background as the sample 0659 but the center region is non-hysterical.

magnetization won't change significantly before the moments start to flip vertically when in-plane domains provide a suitable closure environment to reduce the energy cost of out-of-plane flip at position 3. The resistance at position 3 is already relatively high, because there exist a lot of in-plane domains, whose size will grow with increasing field. With further increase of the field, in-plane domains keep growing to reduce the energy cost of the vertical flip of the magnetization until position 4, where the magnetization is alomost zero and the resistance reaches a maximum because of the maximum of the domain wall density. The system will return to a low resistance state if the field keeps increasing to the positive saturation field to destroy all the domain walls at position 5. The data of in-plane magnetoresistance is plotted in figure 4.28. Together with the corresponding in-plane M-H hysteresis loop, one can track the in-plane switching of magnetic domains.

The sample has no domain walls and is therefore in a relatively low resistance state at position 1. At position 2, some magnetic moments start to flip within the plane and create the environment for moments flip to out-of-plane to reduce the total energy of the system at position 3. Those flipped domains will keep growing with the increase of the field and the resistance will reach a maximum at position 4. When the field increases to the saturation field, all domain walls will be destroyed and the sample will switch back to the relatively low resistance state at position 5.
Both in- and out-of-plane magnetoresistance measurements show that the domain wall resistance for the low PMA sample 0663 is not only proportional to the domain wall density, but also proportional to the domain size during the switching. In contrast to the high PMA sample, the easy axis of the low PMA sample lies in-plane, which leads to a narrower in-plane magnetization curve as shown in figure 4.28. Therefore, the

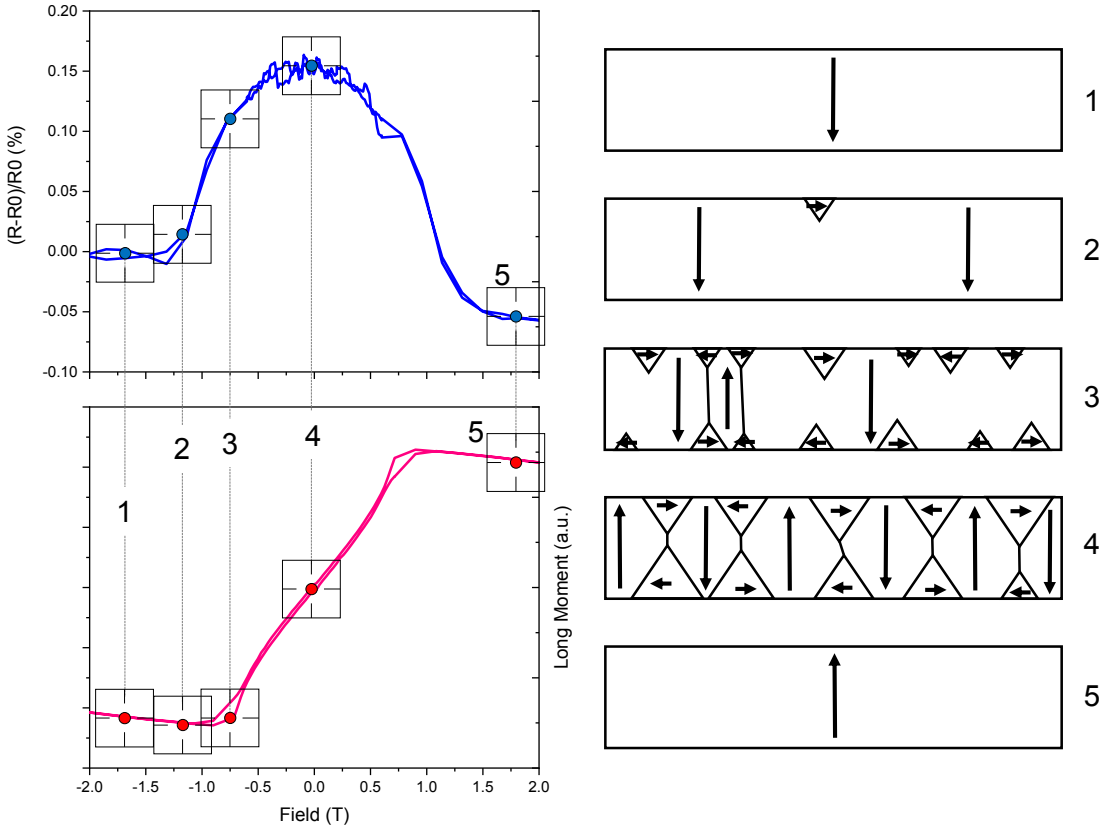

Figure 4.27: The out-of-plane magnetoresistance and corresponding magnetic hysteresis loop of the sample 0663 with low PMA (left). Lateral domain structure at different stages during the magnetization switching (right).

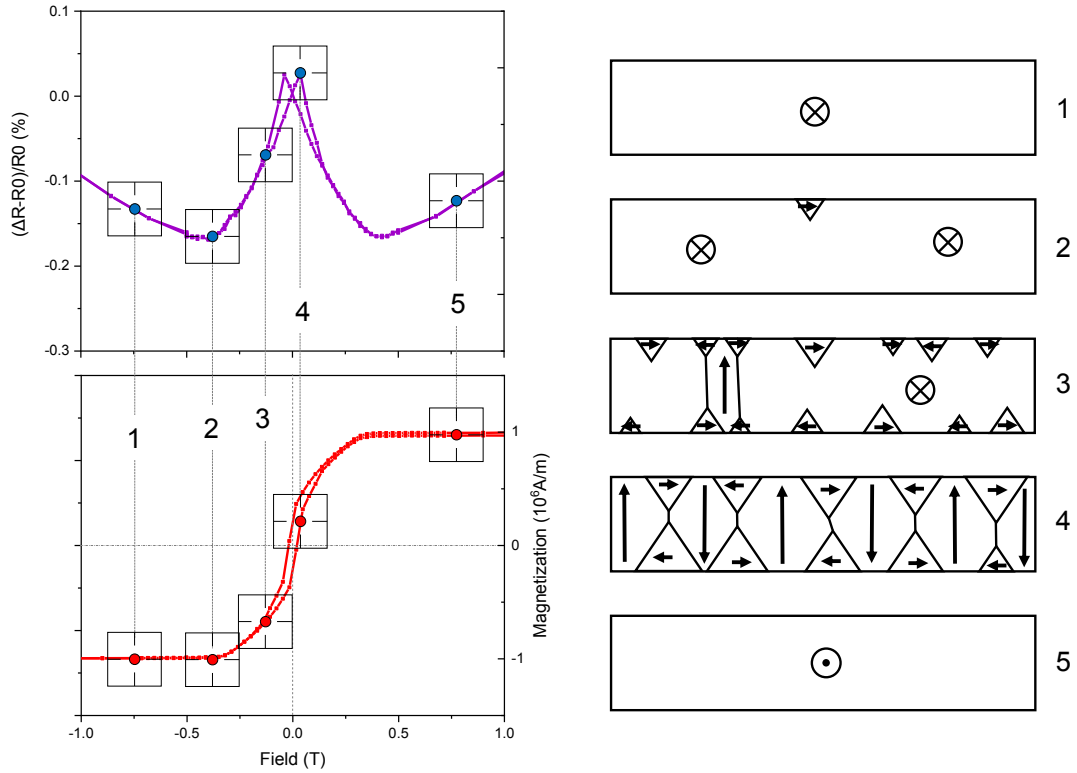

Figure 4.28: The in-plane magnetoresistance and corresponding magnetic hysteresis loop of the sample 0663 with low PMA (left). Lateral domain structure at different stages during the magnetization switching (right).

curve of out-of-plane magnetoresistance measurement is wider than that of in-plane magnetoresistance measurement as shown in figure 4.27 and 4.28. Amplitudes of the in- and out-of-plane are both around 0.16%, which are much lower than the amplitudes of measurements of high PMA sample. In addition, the domain wall density of the low PMA sample after demagnetization is higher than that of high PMA sample after demagnetization as shown in figure 4.29. Therefore, the contribution of one domain wall to the magnetoresistance for high PMA sample is much higher than the contribution of one domain wall to the magnetoresistance for low PMA sample. As shown in figure 4.24 and 4.27, the main component of domain walls of high PMA and low PMA sample is Bloch wall and Néel Wall, respectively. Thus, the contribution of Bloch wall to the magnetoresistance is higher than that of Néel Wall.

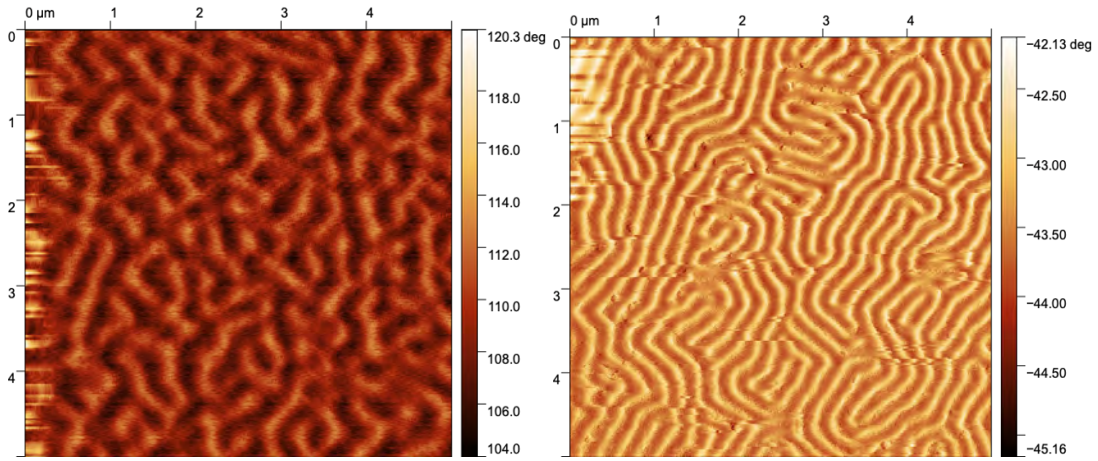

(a) (b)

Figure 4.29: 5×5 μm MFM images of high PMA (a) and low PMA (b) after out-of-plane demangetization. The domain wall density of high PMA sample is much lower than that of low PMA sample.

5 Summary

This project is a supplementary study on magnetic domains of FePd thin films in Annika Stellhorn's PhD thesis, in which FePd thin films with various PMA have been grown by using co-deposition and shuttered growth methods under different conditions. Films with strong PMA exhibit maze domain structure as there is no preferred in-plane orientation, while low or weak PMA results in a parallel striped domain structure. Neutron scattering was also carried out to observe the depth-profile of magnetic domains in the FePd layer.

In this project, we have managed to grow FePd thin films with equivalent qualities without the Cr seed layer between MgO substrate and Pd buffer layer. From the XRD and the magnetization measurements one can conclude that the Cr seed layer only enhances the long-range order of the FePd layer but barely influences the uniaxial quality factor Q.

Two samples with strong PMA and low PMA were grown by using the co-deposition and the shuttered growth method in the OMBE system, respectively. The in-situ characterization method RHEED was used to monitor the growth process and the surface crystalline property was checked by using the LEED installed in the buffer layer of the OMBE system. XRD and WAXS measurements were performed to analyze the crystalline structure as well as the long-range order and the in-plane crystalline structure of the sample. The results show that the long-range order parameter of the sample grown with co-deposition method reaches 0.375, while the parameter of the sample grown with shuttered growth method is 0.

The sample grown with co-deposition method exhibits strong PMA and the shuttered growth method leads to low PMA, which is determined by SQUID magnetization measurements. MFM measurements show that the sample with strong or high PMA has a maze domain structure with an average domain width of 186.5±28 nm, while the weak or low PMA sample exhibits a parallel domain pattern with an average domain width of 86.3±6.1 nm. Together with the layer thicknesses determined by XRR measurements, a simplified model of magnetic domains can be built for both samples.

Magnetoresistance measurements were carried out to investigate the switching mechanism of magnetic domains. The result shows that the magnetoresistance is proportional to the domain wall density and for the sample with low PMA the domain wall density is also proportional to the size of closure domains. Based on the magnetoresistance data, a model of switching process was built for both samples.

6 Outlook

In this project, the lateral magnetic domain structure of FePd thin film including the closure domain is determined phenomenological via MFM images and magnetization measurements. There are several characterization methods that can analyze the lateral domain structure directly, e.g. the Lorentz transmission electron microscopy is a powerful tool to study the magnetic domain structure. No information on the domain walls structure was obtained from those measurements. Such information can be obtained by polarized neutron scattering under grazing incidence [35].

7 Acknowledgments

This project would not have been possible without the support of my colleagues. Here I would like to express my sincere gratitude to the following people.
Prof. Dr. Thomas Brückel for providing me this wonderful opportunity to work at JCNS-2. **Prof. Dr. Regina Dittmann** for willing to be my second second supervisor.
Also, I would like to thank **Dr. Emmanuel Kentzinger**, **Dr. Connie Bednarski-Meinke** and **Dr. Mai Hussein** for all the support and discussions and constructive suggestions every weeks during last 6 month.
Annika Stellhorn and **Patrick Schöffmann** for providing lots of suggestions on optimized growth parameters of the OMBE system and the introduction of the AFM system.
PD Dr. Oleg Petracic, **Dr. Shibabrata Nandi** and **Dr. Ulrich Rücker** for the safety instructions on the MPMS system, the PPMS system and the X-ray lab.
Hengbo Zhang for helping me out of the XRR data evaluation and the operation of the XRD instrument.
I want to thank all the members at JCNS-2 for the creative daily atmosphere during this challenging corona-virus pandemic.
At last I would like to especially thank my girlfriend, family and friends for their support and encouragement.

Bibliography

[1] D. E. Laughlin, K. Srinivasan, M. Tanase, and L. Wang. "Crystallographic aspects of L10 magnetic materials". In: *Scripta Materialia* 53.4 (Aug. 2005), pp. 383–388. DOI: 10.1016/j.scriptamat.2005.04.039.

[2] G. Beutier, G. van der Laan, K. Chesnel, A. Marty, M. Belakhovsky, S. P. Collins, E. Dudzik, J.-C. Toussaint, and B. Gilles. "Characterization of FePd bilayers and trilayers using soft x-ray resonant magnetic scattering and micromagnetic modeling". In: *Physical Review B* 71.18 (May 2005). DOI: 10.1103/physrevb.71.184436.

[3] M. Nakayama, T. Kai, S. Ikegawa, H. Yoda, and T. Kishi. *Magnetoresistance effect element and magnetic random access memory*. US Patent 8,279,663. Oct. 2012.

[4] M. Viret, Y. Samson, P. Warin, A. Marty, F. Ott, E. Søndergård, O. Klein, and C. Fermon. "Anisotropy of Domain Wall Resistance". In: *Physical Review Letters* 85.18 (Oct. 2000), pp. 3962–3965. DOI: 10.1103/physrevlett.85.3962.

[5] V. Gehanno, A. Marty, B. Gilles, and Y. Samson. "Magnetic domains in epitaxial ordered FePd(001) thin films with perpendicular magnetic anisotropy". In: *Physical Review B* 55.18 (May 1997), pp. 12552–12555. DOI: 10.1103/physrevb.55.12552.

[6] C. Clavero, J. M. Garcia-Martin, J. L. C. Krämer, G. Armelles, A. Cebollada, Y. Huttel, R. A. Lukaszew, and A. J. Kellock. "Temperature and thickness dependence at the onset of perpendicular magnetic anisotropy inFePdthin films sputtered onMgO(001)". In: *Physical Review B* 73.17 (May 2006). DOI: 10.1103/physrevb.73.174405.

[7] S. Blundell. *Magnetism in Condensed Matter*. OXFORD UNIV PR, Dec. 1, 2001. 238 pp. ISBN: 0198505922. URL: https://www.ebook.de/de/product/2766192/stephen_blundell_magnetism_in_condensed_matter.html.

[8] Morrish. *Physical Principles Magnetism IEEE Reiss*. John Wiley & Sons, Jan. 1, 2001. 700 pp. ISBN: 078036029X. URL: https://www.ebook.de/de/product/3616765/morrish_physical_principles_magnetism_ieee_reiss.html.

[9] M. T. Johnson, P. J. H. Bloemen, F. J. A. den Broeder, and J. J. de Vries. "Magnetic anisotropy in metallic multilayers". In: *Reports on Progress in Physics* 59.11 (Nov. 1996), pp. 1409–1458. DOI: 10.1088/0034-4885/59/11/002.

[10] J. M. D. Coey. *Magnetism and magnetic materials*. Cambridge New York: Cambridge University Press, 2009. ISBN: 9780511677434.

[11] T. Ichitsubo and K. Tanaka. "Single-crystal elastic constants of disordered and ordered FePd". In: *Journal of Applied Physics* 96.11 (Dec. 2004), pp. 6220–6223. DOI: 10.1063/1.1809775.

[12] A. Belsky, M. Hellenbrandt, V. L. Karen, and P. Luksch. "New developments in the Inorganic Crystal Structure Database (ICSD): accessibility in support of materials research and design". In: *Acta Crystallographica Section B Structural Science* 58.3 (May 2002), pp. 364–369. DOI: 10.1107/s0108768102006948.

[13] M. Futamoto, M. Nakamura, M. Ohtake, N. Inaba, and T. Shimotsu. "Growth of L10-ordered crystal in FePt and FePd thin films on MgO(001) substrate". In: *AIP Advances* 6.8 (Aug. 2016), p. 085302. DOI: 10.1063/1.4960554.

[14] A. Stellhorn, A. Sarkar, E. Kentzinger, M. Waschk, P. Schöffmann, S. Schröder, G. Abuladze, Z. Fu, V. Pipich, and T. Brückel. "Control of the stripe domain pattern in L10-ordered FePd thin films". In: *Journal of Magnetism and Magnetic Materials* 476 (Apr. 2019), pp. 483–486. DOI: 10.1016/j.jmmm.2018.12.059.

[15] H. A. Dürr. "Chiral Magnetic Domain Structures in Ultrathin FePd Films". In: *Science* 284.5423 (June 1999), pp. 2166–2168. DOI: 10.1126/science.284.5423.2166.

[16] G. van der Laan, K. Chesnel, M. Belakhovsky, A. Marty, F. Livet, S. Collins, E. Dudzik, A. Haznar, and J. Attané. "Magnetic anisotropy of aligned magnetic stripe domains in FePd studied by soft x-ray resonant magnetic scattering, magnetic force microscopy and micromagnetic modeling". In: *Superlattices and Microstructures* 34.1-2 (July 2003), pp. 107–126. DOI: 10.1016/j.spmi.2004.01.005.

[17] J. Reichow. *Technical System Description of DCA MBE M600 Molecular Beam Epitaxy System*. Jan. 2010.

[18] U. Latif, S. Can, O. Hayden, P. Grillberger, and F. L. Dickert. "Sauerbrey and anti-Sauerbrey behavioral studies in QCM sensors—Detection of bioanalytes". In: *Sensors and Actuators B: Chemical* 176 (Jan. 2013), pp. 825–830. DOI: 10.1016/j.snb.2012.09.064.

[19] E. N. Kaufmann. *Characterization of Materials. 3 Volume Set*. Wiley John + Sons, Jan. 1, 2013. 2438 pp. ISBN: 1118110749. URL: https://www.ebook.de/de/product/18918526/elton_n_kaufmann_characterization_of_materials_3_volume_set.html.

[20] M. Waschk. "Interface phenomena in La1/3Sr2/3FeO3/La2/3Sr2/3MnO3 heterostructures and a quest for p-electron magnetism". PhD thesis. RWTH Aachen University, 2017.

[21] A. Glavic. "Multiferroicity in oxide thin films and heterostructures". PhD thesis. RWTH Aachen University, 201.

[22] M. Björck and G. Andersson. "GenX: an extensible X-ray reflectivity refinement program utilizing differential evolution". In: *Journal of Applied Crystallography* 40.6 (Nov. 2007), pp. 1174–1178. DOI: 10.1107/s0021889807045086.

[23] E. Kentzinger, M. Krutyeva, and U. Rücker. "GALAXI: Gallium anode low-angle x-ray instrument". In: *Journal of large-scale research facilities JLSRF* 2 (Mar. 2016). DOI: 10.17815/jlsrf-2-109.

[24] A. Technologies. *User's Guide of Agilent Technologies 5400 Scanning Probe Microscope*. Oct. 2007.

[25] P. Zakalek. "Magnetic Interface Effects in Thin Film Heterostructures". PhD thesis. RWHT Aachen University, 2015.

[26] M. Mcelfresh. "Fundamentals of magnetism and magnetic measurements featuring Quantum Design's magnetic property measurement system". In: *Quantum Design* (1994).

[27] QuantumDesign. *Horizontal Rotator Option User's Manual for Physical Property Measurement system*. Part Number 1384-100B. 2000.

[28] QuantumDesign. *Hardware Manual of the Physical Property Measurement System*. Part number 1070-150, B-1. Quantum Design. 2004.

[29] QuantumDesign. *Resistivity Option User's Manual for Physical Property Measurement System*. 1999.

[30] CrysTec. *Data-Sheet of MgO substrate*. http://crystec.de/daten/mgo.pdf.

[31] P. Dobson, B. Joyce, J. Neave, and J. Zhang. "Current understanding and applications of the RHEED intensity oscillation technique". In: *Journal of Crystal Growth* 81.1-4 (Feb. 1987), pp. 1–8. DOI: 10.1016/0022-0248(87)90355-1.

[32] M. Hellenbrandt. "The Inorganic Crystal Structure Database (ICSD)—Present and Future". In: *Crystallography Reviews* 10.1 (Jan. 2004), pp. 17–22. DOI: 10.1080/08893110410001664882.

[33] E. Owen and E. Yates. "XLI.Precision measurements of crystal parameters". In: *The London, Edinburgh, and Dublin Philosophical Magazine and Journal of Science* 15.98 (Feb. 1933), pp. 472–488. DOI: 10.1080/14786443309462199.

[34] B. E. Warren. *X-Ray Diffraction*. DOVER PUBN INC, June 1, 1990. 400 pp. ISBN: 0486663175. URL: https://www.ebook.de/de/product/3303133/b_e_warren_x_ray_diffraction.html.

[35] A. Stellhorn. "Interaction between ferromagnet and superconductor". PhD thesis. RWTH Aachen University, 2020.

[36] V. Gehanno. "Perpendicular magnetic anisotropy of epitaxial thin films of fep-dordered alloys". PhD thesis. Universite Joseph-Fourier, 1997.

[37] D. Halley, Y. Samson, A. Marty, C. Beign, and B. Gilles. "Surface morphology and chemical ordering in FePd/Pd(001) thin layers". In: *Surface Science* 481.1-3 (June 2001), pp. 25–32. DOI: 10.1016/s0039-6028(01)01061-5.

[38] O. Hellwig, G. Denbeaux, J. Kortright, and E. E. Fullerton. "X-ray studies of aligned magnetic stripe domains in perpendicular multilayers". In: *Physica B: Condensed Matter* 336.1-2 (Aug. 2003), pp. 136–144. DOI: 10.1016/s0921-4526(03)00282-5.

[39] N. Vukadinovic, H. L. Gall, J. B. Y. V. Gehanno, A. Marty, Y. Samson, and B. Gilles. "Magnetization dynamics and relaxation in epitaxial FePd thin films with a stripe domain structure". In: *The European Physical Journal B - Condensed Matter and Complex Systems* 13.3 (2000), pp. 445–450. ISSN: 1434-6036. URL: https://doi.org/10.1007/s100510050056.

[40] J. R. Skuza, C. Clavero, K. Yang, B. Wincheski, and R. A. Lukaszew. "Microstructural, Magnetic Anisotropy, and Magnetic Domain Structure Correlations in Epitaxial FePd Thin Films With Perpendicular Magnetic Anisotropy". In: *IEEE Transactions on Magnetics* 46.6 (June 2010), pp. 1886–1889. DOI: 10.1109/tmag.2009.2039923.

[41] O. Ersen, V. Parasote, V. Pierron-Bohnes, M. C. Cadeville, and C. Ulhaq-Bouillet. "Growth conditions to optimize chemical order and magnetic properties in molecular-beam-epitaxy-grown CoPt/MgO(001) thin films". In: *Journal of Applied Physics* 93.5 (Mar. 2003), pp. 2987–2995. DOI: 10.1063/1.1538319.

[42] P. M. Levy and S. Zhang. "Resistivity due to Domain Wall Scattering". In: *Physical Review Letters* 79.25 (Dec. 1997), pp. 5110–5113. DOI: 10.1103/physrevlett.79.5110.

[43] C. H. Marrows and B. C. Dalton. "Spin Mixing and Spin-Current Asymmetry Measured by Domain Wall Magnetoresistance". In: *Physical Review Letters* 92.9 (Mar. 2004). DOI: 10.1103/physrevlett.92.097206.

[44] L. Ma, D. A. Gilbert, V. Neu, R. Schäfer, J. G. Zheng, X. Q. Yan, Z. Shi, K. Liu, and S. M. Zhou. "Magnetization reversal in perpendicularly magnetized L10 FePd/FePt heterostructures". In: *Journal of Applied Physics* 116.3 (July 2014), p. 033922. DOI: 10.1063/1.4890936.

[45] D. Ravelosona, A. Cebollada, F. Briones, C. Diaz-Paniagua, M. A. Hidalgo, and F. Batallan. "Domain-wall scattering in epitaxial FePd ordered alloy films with perpendicular magnetic anisotropy". In: *Physical Review B* 59.6 (Feb. 1999), pp. 4322–4326. DOI: 10.1103/physrevb.59.4322.